

# The boundary-layer characteristics and unsteady flow topology of full-scale operational inter-modal freight trains

J. R. Bell<sup>a,b</sup>, D. Burton<sup>a</sup>, M. C. Thompson<sup>a</sup>

<sup>a</sup> *Department of Mechanical and Aerospace Engineering, Monash University, Clayton, Victoria, Australia*

<sup>b</sup> *Deutsches Zentrum für Luft- und Raumfahrt, Göttingen, Germany*

---

## Abstract

The boundary layers that develop at the sides of full-scale operational inter-modal freight trains were measured using rakes of 4-hole dynamic-pressure probes. The average boundary-layer displacement thickness at the middle of the trains measured under low crosswind was 1.6 m (within the range of 0.5–3 m), showing turbulence intensities of 4–13%, and length scales of 5–30 m. These characteristics, together with other quantitative details provided in the paper, are intended to provide insight for future experiments and simulations to model real-world conditions around freight trains. The sensitivity of the boundary layer and flow topology to environmental crosswinds and loading configuration was also investigated. In addition, insight is provided into the unsteady flow topology around freight trains, the frequency content of the induced flow, and correlation characteristics.

---

## 1. Introduction

Inter-modal freight trains in typical operation have lengths of up to 1.6 km, carry a variety of freight container sizes, and travel at up to 110 km/hr. The various container sizes can be double-stacked during transport, as well as carried via different wagon types, resulting in a loading configuration where horizontal gap length and height are variables with a significant range that vary along the length of the train. Efforts are made in practice to optimize the loading configuration for weight distribution and volume efficiency. However, operational conditions also have clear scope for aerodynamic optimization that is not often realised in practice.

The aerodynamics of freight trains are important for the vehicle's overall resistance and, therefore, efficiency. Aerodynamic resistance (drag) can be significantly greater than rolling resistance (Raghunathan et al., 2002, Shetz, 2001). This is primarily due to the steel wheel-rail interface resulting in low rolling resistance and in contrast, the high aerodynamic resistance that arises from the overall make-up of the vehicle; a collection of a number of predominantly bluff components connected in series. In addition, the crosswind stability of a train and its components are a critical aerodynamic characteristic that concerns

15 the safety of the operators, as well as nearby civilians and infrastructure. Thus, there has been significant  
16 research into the aerodynamics of freight trains, with full-scale experiments (Lai and Barkan, 2005, Lai  
17 et al., 2008, Lukaszewicz, 2007, 2009, Gallagher et al., 2018), scaled wind-tunnel experiments (Li et al.,  
18 2017, Watkins et al., 1992, Engdahl et al., 1986, Gielow and Furlong, 1988, Storms et al., 2008, Peters,  
19 1993), scaled moving-model experiments (Soper et al., 2014) and Computational Fluid Dynamic (CFD)  
20 simulations (Östh and Krajnović, 2014, Maleki et al., 2017, 2019, Flynn et al., 2014, 2016, Hemida and  
21 Baker, 2010, Gallagher et al., 2018, Paul et al., 2007) having been performed. Such research has established  
22 that there exists scope for aerodynamic optimization of these vehicles. Recommendations for improved  
23 aerodynamic loading configurations have been made (Li et al., 2017, Lai et al., 2008, Lai and Barkan,  
24 2005, Beagles and Fletcher, 2013, Engdahl et al., 1986, Paul et al., 2007), as well as design considerations  
25 of containers and wagons (Watkins et al., 1992, Öngüner, Henning, Fey and Wagner, 2020). Further, insight  
26 into the flow field around these vehicles (Östh and Krajnović, 2014, Soper, 2014, Li et al., 2017, Maleki  
27 et al., 2017, 2019) have provided insight into the causal mechanisms of the forces experienced.

28 Accommodating the operational length to height ratios ( $L/H = 250-500$ ) is a significant difficulty in  
29 accurately modelling the realistic aerodynamic conditions around a freight train. This difficulty arises from  
30 physical limitations in scaled experiments (for example, wind-tunnel test-section length) and computational  
31 resource requirements in numerical simulations. This often results in considerably reduced train lengths  
32 being modelled ( $L/H = 10-50$ ). This difficulty and the induced effects have been acknowledged and  
33 considered in high-speed train aerodynamic investigations, where comparatively moderate length to height  
34 ratios ( $L/H = 25-100$ ) exist (Muld et al., 2013, Bell et al., 2017, 8-11 December, 2014). Beyond the local  
35 flow topology that occurs around the head of the train, (and similarly, prior to the local flow around the tail),  
36 a boundary layer develops over the surface of the vehicle. The developing boundary layer is characterised  
37 by the velocity, turbulence and length-scale profiles.

38 The aerodynamic characteristics of bluff bodies and their geometric features in general have been well  
39 established to be sensitive to the turbulent conditions they are exposed to (Cooper and Campbell, 1981,  
40 Watkins and Cooper, 2007). In wind engineering, accurate modelling of the velocity, turbulence and  
41 length-scale atmospheric boundary-layer characteristics that a building is exposed to is critical for ensuring  
42 accurate prediction of wind loads (Holmes, 2001). Similarly, there have been recent efforts to charac-  
43 terise (Wordley and Saunders, 2008, McAuliffe et al., 2014) real-world on-road turbulence and replicate  
44 these conditions in wind-tunnel and CFD simulations for automotive aerodynamic investigations (Sims-  
45 Williams, 2011). Specifically, the aerodynamic sensitivity of a freight container to the conditions it is  
46 exposed to has been indicated by a number of investigations. A container in isolation has been shown to

47 experience a significantly different flow field, pressure distribution and forces to a container located within  
48 a series of containers (Östh and Krajnović, 2014, Li et al., 2017, Maleki et al., 2017, 2019). Further, the  
49 drag of individual containers have reportedly been found to be dependent on location in the train, only be-  
50 coming consistent at approximately 8 cars from the nose (Gielow and Furlong, 1988, Engdahl et al., 1986).  
51 Thus, there is clear motivation to accurately represent the flow that a shipping container is exposed to, in  
52 order to ensure that the findings from investigations aiming for optimization are correct in their magnitude  
53 and overall effect.

54 A common method in investigations that consider the effect that model length can have on aerodynamic  
55 findings, is to model an arbitrary region within the length of the train, representative of the conditions that  
56 the majority of containers experience (Östh and Krajnović, 2014, Li et al., 2017, Maleki et al., 2017, 2019).  
57 However, the characteristics at this arbitrary *middle* position, until now, have not been defined for opera-  
58 tional freight trains subject to real-world atmospheric conditions. Some insight into these characteristics  
59 has been limited to slipstream-motivated experimental campaigns, which are focussed on accurately mea-  
60 suring the peak induced-velocity caused by trains at a specific position in their immediate vicinity (3m from  
61 the track centre); where waiting passengers, workers or infrastructure can be most strongly affected. With  
62 safety as a motivation, and the resulting European regulations for testing and requirements that must be met  
63 for trains to operate (CEN, 2013), there has been a wide range of research in the area (Sterling et al., 2008,  
64 Soper et al., 2014, Muld et al., 2013, Flynn et al., 2014, 2016, Bell et al., 8-11 December, 2014, 2016b,  
65 2017, Soper and Baker, 2019). However, such research and regulations are not intended to, and therefore  
66 do not properly measure and resolve a train’s boundary-layer characteristics.

67 With further insight into the boundary layer characteristics of operational freight trains, models in  
68 future investigations could be tuned to match realistic oncoming conditions in the same manner as for the  
69 atmospheric boundary layer in the practice of wind engineering. Experimentally, this could be achieved  
70 through boundary-layer augmentation utilizing roughness, tripping and vortex-generating elements (Irwin,  
71 1981, Bell et al., 8-11 December, 2014, Sima et al., 2016, Buhr and Ehrenfried, 2017, Bell et al., 2017).  
72 Similar approaches could be applied numerically, or alternatively, through advanced recycling techniques  
73 (Östh and Krajnović, 2014) or through tuning of inlet conditions.

74 In this work, the characteristics of boundary layers of operational inter-modal freight trains are pre-  
75 sented. Here we use the terminology *boundary layer* in a broad sense to describe the induced flow along  
76 the side of the train and tracks. It may be a combination of turbulent structures generated along the side of  
77 the train, and, in the presence of cross-wind, wake structures over the side of the train. Measurements were  
78 made with 3 horizontal boundary-layer rakes perpendicular to the rail to measure the side boundary-layer.



Figure 1: An operational full-scale inter-modal freight train driving past measurement rakes of 4-hole dynamic pressure probes, placed either side of the train.

79 Each rake contained 7 four-hole dynamic pressure probes. A vertical rake of 3 probes was also utilized  
80 to investigate the boundary layer's three-dimensionality. In addition to quantifying the boundary layers,  
81 insight into the flow physics around inter-modal shipping containers and their loading configurations is  
82 presented.

83 Measurements of six inter-modal freight trains were performed, each effectively measured three times  
84 by each of the horizontal rakes. Inter-modal freight trains have no standard, consistent configuration.  
85 Therefore, each train had different loading configurations and further, operated within different environ-  
86 mental conditions. It is acknowledged this is a small sample size that does not result in a statistically  
87 significant description of a benchmark-type boundary-layer for a specific train. However, these measure-  
88 ments — for the first time — enable the boundary layer characteristics representative of real, inter-modal  
89 freight trains operating in real conditions to be described. These results provide valuable insight into real-  
90 world operational conditions and hence can be used to help inform setting up wind-tunnel experiments  
91 and numerical simulations that investigate the aerodynamics of freight trains. This work is part of a col-  
92 laboration with Pacific National — a freight transport provider — with the ultimate aim of improving the  
93 aerodynamic efficiency of inter-modal freight transport

## 94 **2. Methodology**

### 95 *2.1. Test site*

96 The experiment was performed at Wingeel, Victoria, Australia. The standard-gauge track network that  
97 inter-modal freight trains operated within proximity to Melbourne was assessed for aerodynamic and logis-  
98 tical considerations. The Wingeel test site was identified as suitable, utilizing Pacific Nationals expertise  
99 as a transport operators.

100 The test site consisted (Fig. 1) of a single track, which allowed access and simultaneous measurement  
 101 along both sides of the train without having to consider rail traffic on a parallel track. Trains operate at  
 102 full operational speed ( $u_t \approx 110$  km/hr) and were given prior notice of the experiment and infrastructure  
 103 setup to maintain the maximum speed during passage past the data collection infrastructure. The track is  
 104 relatively straight (Fig. 2), which enabled a straight vehicle passing the measurement equipment to operate  
 105 at maximum speed.

106 A minor highway was located approximately 1 km north of the test site. At this distance, the effect  
 107 of passing automotive vehicles on the measurements was expected to be negligible. A minor local road  
 108 crossed the railway 50 m east of the test site and contained minimal traffic infrastructure (lights/sirens)  
 109 mounted on poles. This road experienced minimal traffic, and vehicles if present were stationary and  
 110  $\approx 10$  m from the track during measurements of the trains. This configuration is not expected to have  
 111 significantly shielded the measurement devices from the induced flow of the trains being measured, and  
 112 thus not expected to have a significant influence on the results.

113 The local topography was relatively flat, and clear of trees and vegetation. Minimal local topography  
 114 was desired, to best represent the ideal conditions of the rail vehicle operating in open air. This of course  
 115 opened the site and vehicle to be exposed to ambient wind, however, those conditions were measured.



Figure 2: The experiment test site at Wingeel, Victoria, Australia. A large-scale view of the track and roads are illustrated (top), with the local topography and location of trees and vegetation illustrated in the zoomed-in figure inset below.

116 2.2. Test vehicles & conditions

117 The passing of inter-model freight trains in normal operation were recorded in the experiment. Only  
 118 single-stacked shipping containers existed on the trains subject to measurement. A variety of loading  
 119 configurations, in terms of gap sizes between containers, existed within each train measured, and indeed  
 120 between all trains in the set. In Figure 3, the extent of gap variation is visible. Figure 3a illustrates how  
 121 containers can be positioned with no gap between them when loaded on the same wagon. Also in Figure 3a,  
 122 a small gap is visible that is required when containers are loaded on sequential wagons, due to the distance  
 123 required by the coupling between wagons which also provides the ability for the train to operate through  
 124 curves. In Figure 3b, a ‘fractional’ gap is visible. These occur due to the mismatch between available  
 125 space on the wagon for loading, and the size of the container(s) loaded onto this space (referred to as slot  
 126 utilization). In Figures 3c and d, gaps in the order of a full sized container or larger are visible. These occur  
 127 as it is common practice for sets (typically of 5) of multiple wagons to be grouped and moved together.  
 128 When these groups are loaded and added to make a full train, such gaps can exist due to un-required or  
 129 unsuitable space on the wagon for more containers.

130 In this experiment, 6 inter-modal trains were measured. The train number, loading configuration de-  
 131 scription (quantified loading configuration is presented in Section 3.2), and test conditions: train speed  $u_t$ ,  
 132 ambient wind speed,  $u_a$ , absolute ambient-wind yaw-angle  $\gamma$ , and relative ambient-wind yaw-angle  $\beta$  (both  
 133 angles being around the z-axis), are presented in Table 1. The effects of these characteristics are discussed  
 134 in the results section.

Table 1: Test Vehicles and Test Conditions

No.	Test Vehicles		Test Conditions		
	Gap Sizes	$u_t^1$ (m/s)	$u_a^1$ (m/s)	$\gamma$ (°)	$\beta$ (°)
T1	Small-Very Large	30.7	2.3	-4	-0.3
T2	Small-Medium	32.7	3.0	20	2.0
T3	Small-Large	31.1	4.0	12	1.8
T4	Small-Medium	29.9	4.4	149	3.9
T5	Medium-Very Large	24.5	5.0	-48	-9.9
T6	Small-Medium	26.1	7.0	-137	-8.7

135 2.3. Setup

136 The measurement equipment was arranged at the Wingeel site and measurements were obtained as  
 137 the trains passed by them as presented in Fig 1. The experimental setup of the measurement equipment  
 138 and data acquisition is illustrated in Figure 4, with photos of the setup and specific equipment provided in  
 139 Figure 5.

140 The primary pieces of measurement equipment were 4-hole dynamic-pressure probes, positioned in  
141 three rakes (R1, R2 & R4 in Fig. 4) of 7 probes, arranged perpendicular to the path of the trains. The probe  
142 nearest to the train was located 2.5 m from the nearest rail, which corresponds to  $y = 1.71$  m from the  
143 surface of a shipping container travelling on a wagon on the rail. The subsequent probes were positioned at  
144  $\Delta y = 1$  m increments in the horizontal direction. The probes were positioned  $z = 2.1$  m above the top of  
145 rail, which corresponds to approximately half the container height. This setup was consistent for all three  
146 rakes, where rakes R1 & R2 were positioned at the same distance along the track, on either side (Fig 5(a))  
147 in order to provide insight into the correlation and coherence of the flow around the trains. Rake R4 was  
148 positioned on the same side as R1,  $\Delta x = 30$  m away.

149 Rake R3 contained 4 horizontal probes positioned in the manner described above, with 3 probes po-  
150 sitioned in the vertical direction at  $\Delta z = 0.5$  m increments, instead of the furthest 3 horizontal positions  
151 (Fig 5(c)). These were positioned to gain insight into the vertical velocity gradient of the boundary layers.

152 Inside each equipment case were 32 channel Data Acquisition (DAQ) cards that were connected over  
153 the large distances to a laptop via Ethernet cables. Data was acquired at a sampling frequency of 1000  
154 Hz, with sampling times of approximately 140 seconds. Power was supplied to the DAQ and measurement  
155 equipment by a battery. A laptop and the battery were charged using a portable generator; however, during  
156 actual measurement times they were disconnected from the generator and ran solely on battery power, to  
157 remove the possible effect of electrical noise caused by the generator.

158 The event of a train passing, and the position relative to the train nose were measured using two infra-  
159 red transmitter/receivers mounted on vertical supports of the 4-hole probes closest to the rail in rakes R1  
160 and R3 (Fig 5(d)). On the opposite side of the track was a reflective square element that reflected the  
161 transmitted infra-red light to the receiver (Fig 5(e)). When the path (illustrated in Fig 4(a) as red lines)  
162 was broken, a voltage change was measured in additional DAQ cards, thus each unit and reflector will be  
163 subsequently referred to as a 'light gate'. The primary purpose of this equipment was to measure the train  
164 speed. However, these devices also provided insight into the loading configuration, as the light path was  
165 positioned at the height of the shipping containers, thus gaps between containers were recorded.

166 The ambient wind magnitude,  $u_a$ , and direction and temperature were measured at a  $100\text{Hz}$  sampling  
167 rate by a weather station with an ultra-sonic anemometer. This was located on the vertical support of the  
168 probe furthest from the track in rake R1 (Fig 5(a)).

a. Freight - Fully Loaded



b. Freight - Fractional Gaps



c. Freight - Container Gaps



d. Freight - Multiple Container Gaps



Figure 3: Variety of gap sizes between shipping containers observed on the different operational freight trains.

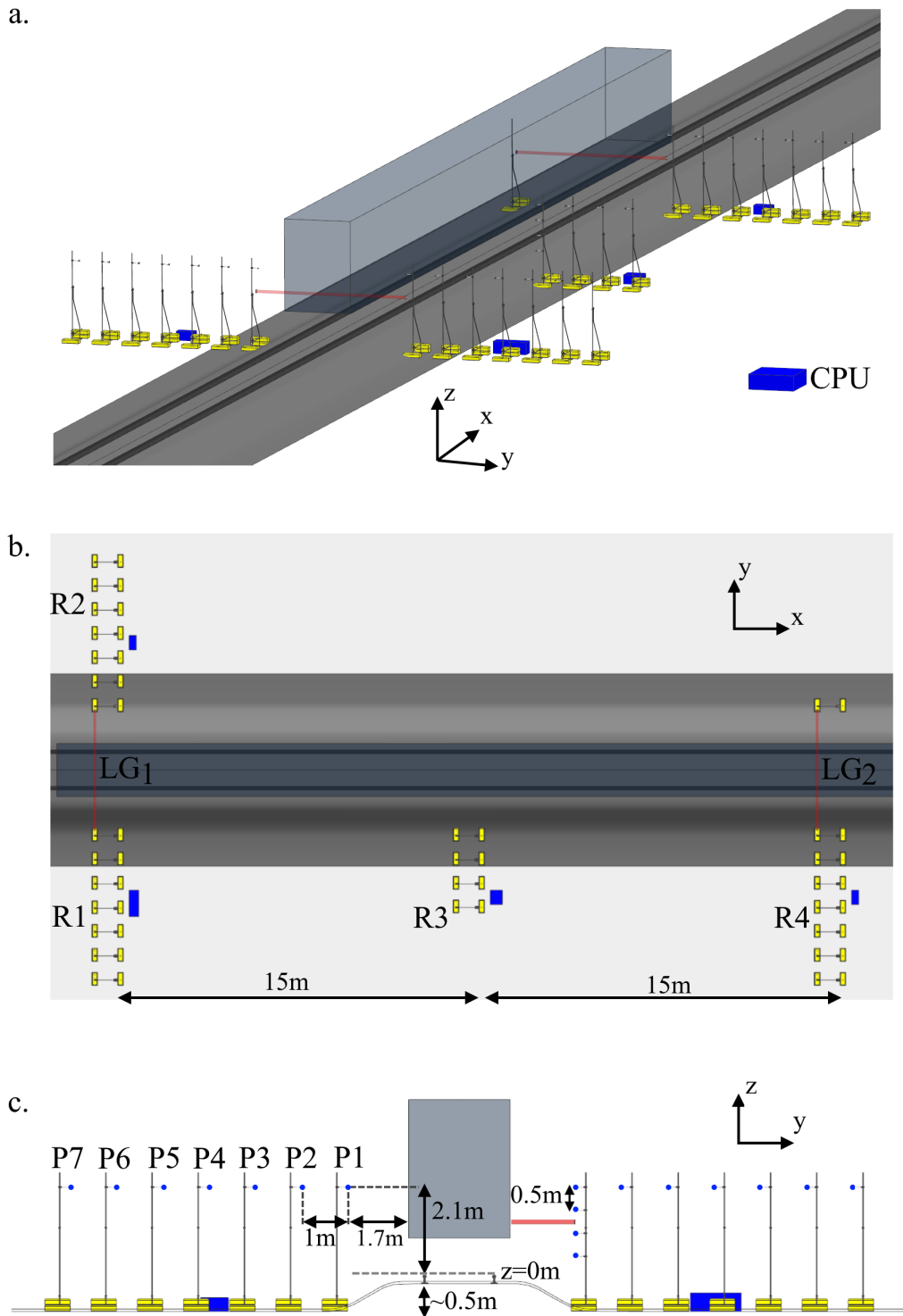


Figure 4: Experimental setup: rakes (R1-R4) of 4-hole dynamic-pressure probes (P1-P7), light-gates (LG1-2) and light-beam paths (red), processing area (CPU) and data acquisition and measurement equipment boxes (blue) presented in (a), isometric, (b): top down, and (c): front-on perspectives.

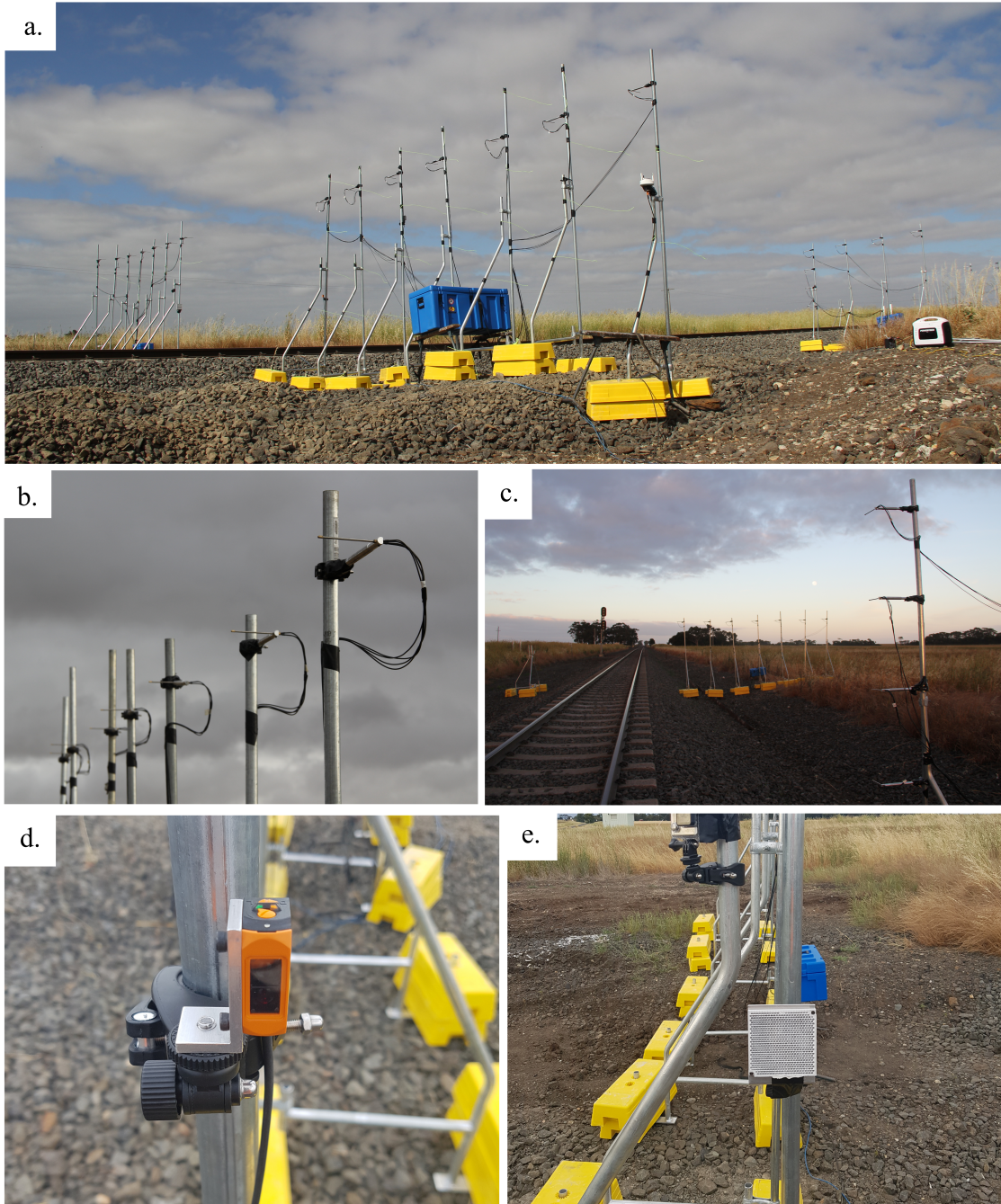


Figure 5: Photos of the setup and experimental equipment. (a): rakes R1 and R2, probe support infrastructure and data acquisition boxes, (b): rake of probes, (c): vertical rake R3, (d): light-gate transmitter/receiver and (e): reflective element for light-gate.

169 2.3.1. Flow velocity

170 The velocity induced by the train's movement was measured by 4-hole dynamic-pressure probes. These  
171 were designed, manufactured and calibrated by the *Monash University Wind Tunnel Platform*, and have  
172 previously been used – and the results published – in a scaled wind-tunnel experiment investigating the  
173 unsteady wake of high-speed trains (Bell et al., 2016a). The 100 mm long probes were positioned  $\Delta y =$   
174 200 mm away from the primary vertical support and mounted in 14 mm diameter horizontal cylinders to  
175 reduce the interference the probe mounting could have on measurements. The mounting configuration of  
176 the probes is visible in Fig 5(b).

177 The probes have a cone of acceptance of  $\pm 45^\circ$ , and therefore were rotated to face the direction of the  
178 oncoming train (facing opposite to the direction the trains were travelling) in order to measure the flow  
179 induced by the trains' surfaces. The probes have an accuracy of approximately  $\pm 1\text{m/s}$  and  $\pm 1^\circ$ . Flow that  
180 was beyond the cone of acceptance ( $< 5\%$ ) was identified in processing through inspection of the pressure  
181 magnitude, sign, and pressure relative to the other holes on the probe. The pressure of each hole was  
182 measured with a differential pressure transducer referenced to atmospheric pressure. Atmospheric pressure  
183 was measured by a reference port connected to a plenum shielded in a container with small vents (to allow  
184 ambient pressure to exist within the container) located at each rake, within a protective equipment case that  
185 was also vented to the atmosphere.

186 Within each equipment case, located at each rake (see blue boxes in Fig 4), was a 32 channel *Dynamic*  
187 *Pressure Measurement System* (DPMS). Each hole of each probe was connected to a transducer in the  
188 DPMS by 4 m of 1.2 mm internal diameter Poly-Vinyl-Chloride (PVC) tubing.

189 The phase and amplitude of the pressure measured by the transducer is subject to distortion relative to  
190 the true pressure at the desired measurement point. This distortion occurs due to resonant characteristics of  
191 the system (Iberall, 1950). The amplitude and phase response for each measurement was corrected using  
192 the inverse transfer function (ITF) method (Irwin et al., 1979). The frequency response of the pressure  
193 measurement system was determined theoretically using a method outlined by Bergh and Tijdeman (1965).  
194 The system had no peak frequencies, and fell below an amplitude of 0.2 at 60 Hz. Beyond this frequency  
195 correction was not applied, in order to reduce the chance of noise amplification.

196 Dynamic-pressure probes were utilized instead of ultra-sonic anemometers - more commonly used in  
197 slipstream motivated investigations (Sterling et al., 2008) – initially due to cost and availability. More  
198 importantly, the use of a large number of probes resulted in a spatial resolution able to reasonably resolve  
199 the boundary layer, take simultaneous measurements either side of the track, and at different longitudinal  
200 locations – effectively measuring the passing of the same train 3 times.

201 *2.3.2. Train velocity & position*

202 As the two light gates were positioned 30 m from each other in rakes R1 and R4, the difference in time  
203 ( $\Delta t$ ) between the two light gates of the increase/decrease caused by the the train's nose and tail passing in  
204 the output voltage signal was used to determine the train speed.

205 An example of the voltage signals of both light-gates is presented in Figure 6(a). Here, the events of  
206 the step-up caused by the nose passing, and subsequent step-down as the tail moves past, are visible, as is  
207 light-gate 1 signal, clearly lagging light-gate 2 (the train was travelling West in this example). Figure 6(b)  
208 shows the voltage of the pressure transducer from the probes closest to the track within each rake. Again,  
209 the lag of the head-pressure pulse is clearly visible due to the spatial offset of the probes location. The train  
210 velocity was calculated by

$$u_t = \frac{x_{LG_1} - x_{LG_2}}{t_{LG_1} - t_{LG_2}}, \quad (1)$$

211 where the longitudinal position of light gates  $LG_1$  and  $LG_2$ ,  $x_{LG_1, LG_2}$  were set and thus known in the  
212 experimental setup, and the times when the train nose passes  $LG_1$  and  $LG_2$ ,  $t_{LG_1, LG_2}$ , were determined  
213 from the light-gate measurements.

214 The train velocity was calculated twice for each passage, using the nose and tail passing events sep-  
215 arately. This enabled the acceleration to be calculated. In all cases, the train acceleration was minimal  
216 ( $a_t < 0.1 \text{ m/s}^2$ ), likely due the minimal separation distance between the light-gates relative to the scale  
217 of the train and track. As such the train speed  $u_t$  was simply taken as the speed calculated from the nose  
218 passing, without acceleration being considered. This train speed was used to convert the data from the  
219 temporal to the spatial domain. All data was then re-sampled to a common spatial resolution, and aligned  
220 relative to the train nose ( $x = 0$ ).

221 *2.3.3. Flow visualisation*

222 Additional insight into the induced flow field as the trains moved through the test site was achieved  
223 with high-visibility yellow wool-tufts. The wool tufts were fixed to the vertical support structures in rake  
224 R1, at each spanwise probe position and at multiple heights. It was expected they influenced by the support  
225 geometry to a degree. However, the tufts are able to indicate flow in all horizontal directions (they don't  
226 have a limited cone of acceptance angle as the pressure probes do), thus they provide complimentary  
227 qualitative results.

228 Photos of the wool tufts were obtained with a digital single-lens-reflex (DSLR) *Canon 60D* camera,  
229 with a focal length of 18 mm, f-stop of f/5.6, exposure time of 1/500 seconds, and frame rate of 4 Hz.

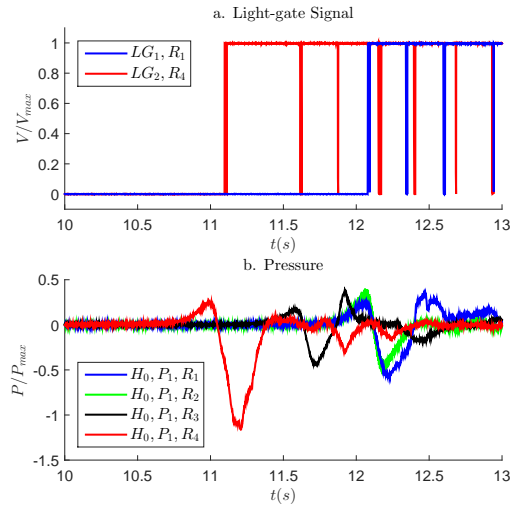


Figure 6: (a): Normalised voltage signal from light-gates LG1 and LG2. (b): Normalised pressure signals from the centre hole ( $H_0$ ) of each of the probes closest to the train (P1) within each rake (R1-R4).

### 230 3. Results

231 The results of an individual train are presented first, to provide initial insight into the measurements  
 232 obtained and the processing techniques applied. The boundary layer characteristics of all trains are then  
 233 presented and compared, followed by the specification of a ‘characteristic boundary layer’, representative  
 234 of an average train operating under minimal crosswind. Finally, insight into global and local flow features  
 235 are presented through flow mapping, frequency and correlation analysis.

#### 236 3.1. Velocity profiles

##### 237 3.1.1. Horizontal arrays

238 In this experiment, the flow induced by the train’s movement is measured, thus induced velocity is  
 239 highest, closest to the surface. The longitudinal velocity ( $u$ ) measured by each of the 7 probes in the  
 240 horizontal rake, R1, for train T3, is shown in Figure 7. These results are representative of the trains (T1,  
 241 T2, T3) measured with low crosswind;  $u_a < 4$  m/s (relative yaw angle,  $\beta < 2^\circ$ ). The differences between  
 242 the velocity measured at the different rakes (R1, R2, R4) are presented and discussed in the following  
 243 sections. The velocity was filtered with a 1 second moving-average window for clarity.

244 The boundary layers around the freight trains are not simply two-dimensional, indeed, nor are they  
 245 necessarily boundary layers in the purest sense. However, they are analysed here as 2D boundary layers  
 246 here for simplicity, as previous researchers have done (Muld et al., 2013, Baker, 2010, Bell et al., 2015).  
 247 Thus, the longitudinal velocity ( $u$ ) is of primary focus as it contributes most significantly to boundary  
 248 layer flow (in this case also). The other velocity components are analysed in Section 3.3. Further, the

249 flow is characterised in later sections with 2D boundary-layer parameters such as displacement thickness  
 250 and shape factor. This enables a level of quantification of boundary layer thickness, and a method for  
 251 comparison across different cases.

252 These results clearly show the existence and increasing thickness of the induced boundary layer along  
 253 the length of the train. This is evident in the velocity being higher at positions close to the train (e.g.  
 254  $y = 1.71$  m) than at positions further away from the train (e.g.  $y = 7.71$  m). Furthermore, it can be  
 255 seen that these induced velocities tend to increase along the length of the train. Significant fluctuations  
 256 in velocity within the boundary layer are largely consistent across the horizontal positions measured. In  
 257 addition, a visible lag in the longitudinal direction exists for the probes further away from the train, caused  
 258 by the flow disturbance requiring time to convect/diffuse to these positions.

259 These results are consistent with research into the slipstream of freight trains by Soper et al. (2014),  
 260 Soper (2014), Sterling et al. (2008) which have also observed increasing induced velocity that reaches a  
 261 maximum along the body – due to the boundary-layer thickness increasing – followed by the significant  
 262 reduction of induced velocity after the tail. This is in contrast to the slipstream of high-speed trains which  
 263 also exhibit increasing velocity along the length due to the boundary-layer thickness increasing, however,  
 264 the highest velocities are found in the near-wake region (Bell et al., 2017, Sterling et al., 2008).

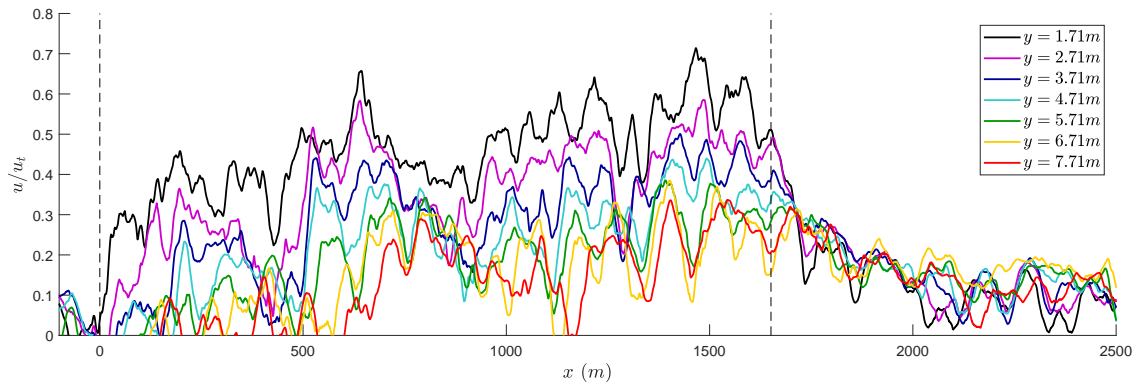


Figure 7: Longitudinal induced velocity,  $u$ , normalised by train speed  $u_t$  measured by each probe in rake R1 for train T3. Dotted vertical lines indicate train nose and tail.

### 265 3.1.2. Vertical array

266 In contrast to the horizontal development of the boundary layer, trends in velocity profile in the vertical  
 267 direction are not as clear. The longitudinal velocity ( $u$ ), measured by each of the 4 probes at a distance of  
 268  $y = 1.71$  m from the train, in the vertical rake, R3, again for train T3, are presented in Figure 8. In general,  
 269 at this position, the velocity is higher at the lower measured positions ( $z = 0.6$  m), closer to the ground,  
 270 than the higher positions ( $z = 2.1$  m). This indicates that the boundary layer is thicker closer to the ground.

271 Such a result is expected, and similar findings have been observed in the literature (Soper et al., 2014). This  
 272 is proposed to be due to the presence of additional elements of the train such as the wheels, bogies, and the  
 273 coupling mechanisms of the wagons. Such elements are likely to increase the entrainment of the ambient  
 274 flow. It is unclear how the ground plane affects the velocity closer to the ground and further away laterally  
 275 from the train, as the lowest measurement was approximately 1.1 metres above the local ground surface.

276 Interestingly, this trend of increasing velocity with increasing height is occasionally inverted, most no-  
 277 tably at  $x = 750m$  in Figure 8. At this point, velocity is highest away from the ground, and decreases  
 278 towards it. There are clear signs of correlation in the velocity fluctuations between the vertically separated  
 279 probes, but perhaps weaker than in the horizontal direction. Together with the inversion of the velocity gra-  
 280 dient this indicates the existence of large-scale, three-dimensional, coherent structures within the boundary  
 281 layer.

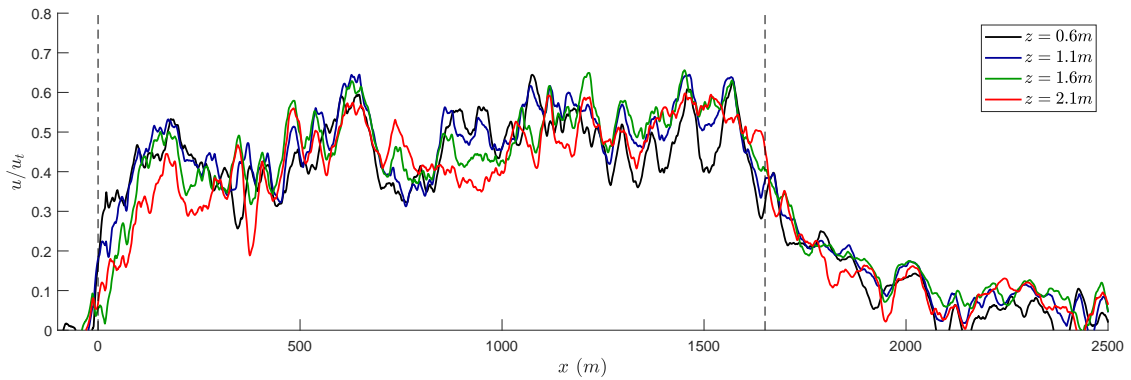


Figure 8: Longitudinal induced velocity,  $u$ , normalised by train speed,  $u_t$ , measured by each probe in the vertical rake R3 for train T3. Dotted vertical lines indicate train nose and tail.

### 282 3.1.3. Horizontal boundary layer profiles

283 Boundary layer profiles at discrete positions along the train are presented in Figure 9. These are de-  
 284 veloped from the same velocity measurements by each of the 7 probes in the horizontal rake, R1, for train  
 285 T3. In this case, the results are presented simply to demonstrate the boundary layer velocity profile. Each  
 286 sequential instantaneous discrete position was selected to illustrate the boundary layer growth along the  
 287 train's length. Significant variation in these instantaneous profiles existed at different locations for the dif-  
 288 ferent trains, as can be expected from the transient velocity profiles in Fig. 7. The boundary layer profile at  
 289 each spatial increment was developed, in order to calculate boundary layer characteristics along the train's  
 290 length. The corresponding characteristics are analysed and the differences between different rakes and  
 291 trains are presented below.

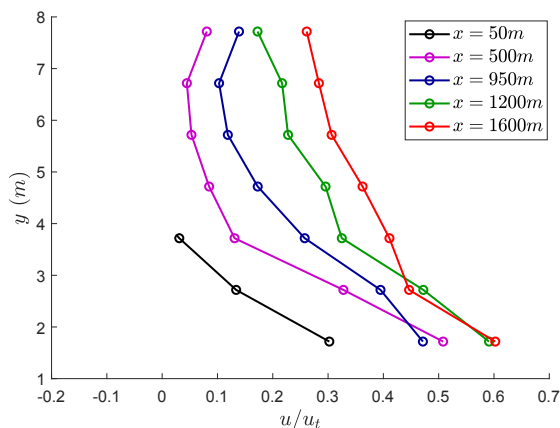


Figure 9: Boundary layer velocity profiles determined from each of the 7 probes in rake R1 at different discrete longitudinal positions along the train.

### 3.2. Boundary-layer characteristics

The characteristics of the boundary layers for each of the 6 trains – low wind, and crosswind exposed trains – are presented and analysed in this section. Following this, a characteristic boundary layer is described, representative of a typical developed boundary layer around an inter-modal freight train. This is intended to help inform setting up experiments and numerical simulations intending to model real-world conditions.

#### 3.2.1. Displacement thickness & shape factor

Utilizing the boundary layer velocity profiles presented above, the displacement thickness was calculated using

$$\delta^*(x) = \int_0^{\infty} \left(1 - \frac{u}{u_t}\right) dy. \quad (2)$$

In Figure 10, the displacement thickness for trains (T1, T2, T3) with low crosswind (relative yaw angle,  $\beta < 2^\circ$ ) are presented. Results from each individual rake (R1, R2, R4) are presented, as well as the ensemble average of all three.

For all three trains, the boundary layer thickness initially increases quickly up to  $\delta^* \approx 1$  m over the first  $\approx 200$  m. Following this, a further, slower development is evident up to a common range of  $\delta^* = 1$ –2 m, within the full range of  $\delta^* = 0.5$ –3.5 m. These values are higher than the range of  $\delta^* = 0.6$ –1.4 m estimated by Soper (2014) in a 1:25 scale moving-model freight-train experiment and  $\delta^* \approx 0.1$  – 0.3 m measured by both Li et al. (2017) in a 1:14.6 scale freight-train wind-tunnel experiment and by Maleki et al. (2017) numerically. Further, these values are an order of magnitude higher than full-scale, operational *high-speed train* boundary layers estimated by Sterling et al. (2008) of  $\delta^* = 0.1$ –0.4 m.

Relative differences between the measurements from the three rakes are also visible in Figure 10. In

312 particular, R1 and R4, positioned on the same side of the train exhibit very similar calculated displacement  
 313 thickness, in contrast to that of R2, positioned on the other side of the train. A possible explanation for  
 314 this, is the influence of the albeit minor crosswind, as the loading configuration is symmetric, and would  
 315 be expected to influence both sides equally. It is for this reason that results from all three rakes are used  
 316 to calculate the ensemble average. Even though it is likely that the measurements from rakes R1 and  
 317 R2 are not independent from each other, as they are positioned at the same longitudinal position. The  
 318 measurements from rake R2 were used in the calculation of averages, to include these differences to better  
 319 represent the ‘average’ boundary layer of the trains measured.

320 The loading configuration of each train is expected to have an influence on the boundary layer that  
 321 develops. In an attempt to quantify the loading configuration along the trains length – in order to compare  
 322 directly the boundary layer displacement thickness – a cumulative blockage parameter was developed. This  
 323 cumulative blockage at each spatial measurement increment,  $i$ , was calculated as

$$x_{B_i} = x_{B_{i-1}} + x_{blocked,i}, \quad (3)$$

324 using the light-gate measurements, where  $x_{blocked,i} = 1$  when the light-gate measured a path blocked by a  
 325 container, or  $x_{blocked,i} = -1$  when the light-gate path was not blocked, thus a gap existed. This parameter  
 326 enables consecutive gaps, or conversely, containers packed closely together, to be visualised.

327 Profiles of cumulative blockage for trains T1, T2, T3 are presented in Figure 11. Comparison of this  
 328 parameter to the corresponding train displacement thickness in Figure 10 shows that the relative changing  
 329 cumulative blockage between the trains tends to match the relative displacement thickness; higher blockage  
 330 (less gaps) approximately corresponds to a thicker boundary layer. Train T1 consistently has the lowest  
 331 displacement thickness and cumulative blockage (the shallower gradient indicates it has small, consistent  
 332 gaps) relative to trains T2 and T3. Further, T2 initially has a large displacement thickness and slightly larger  
 333 cumulative blockage; however, from  $x \approx 600$  m, its blockage and displacement thickness both decrease,  
 334 beyond which both remain lower than T3. Such results indicate loading configuration has an impact on  
 335 the boundary layer, as one could expect; without the effect of crosswind, the boundary layer would be  
 336 expected to increase along the length of the vehicle, sufficiently small gaps could have minor effect or act  
 337 as ‘roughness’, while larger enough gaps would lead to separation of the flow that results in the boundary  
 338 layer re-starting.

339 The shape factor is defined by

$$H(x) = \frac{\delta^*(x)}{\theta(x)}, \quad (4)$$

340 where

$$\theta(x) = \int_0^{\infty} \frac{u}{u_t} \left(1 - \frac{u}{u_t}\right) dy, \quad (5)$$

341 is the momentum thickness. This provides an indication of the form of the boundary layer profile. Profiles  
342 of the shape factor are presented in Figure 12 for the three trains T1, T2, T3. No clear trends exist for the  
343 shape factor over the train lengths, indicating that the boundary layer form is relatively constant. The shape  
344 factor of  $H \approx 1.4$  indicates the boundary layer is turbulent, as expected.

345 The displacement thicknesses of the trains with higher crosswinds: T4 ( $\beta = 4^\circ$ ), T5 ( $\beta = 10^\circ$ ), T6  
346 ( $\beta = -9^\circ$ ), are presented in Figure 13. In this case, the results from the different rakes R1 and R2 are  
347 designated as leeward, (LW), and windward (WW) relative to the crosswind direction.

348 Significant differences are immediately evident with the leeward and windward boundary layers. The  
349 crosswind essentially pushes the boundary layer towards the surface on the windward side, to the point  
350 where the probes are unable to measure a boundary layer. On the leeward side, the calculated displacement  
351 thickness is significantly larger than that observed for the trains with no/little crosswind:  $\delta_{LW:T4,T5,T6}^* =$   
352 2–4 m, compared to  $\delta_{T1,T2,T3}^* = 1\text{--}2.5$  m, respectively. However, complex, three-dimensional flow is  
353 expected on the leeward side, not a simple structureless boundary layer, in which case the calculation of  
354 the displacement thickness is not entirely meaningful.

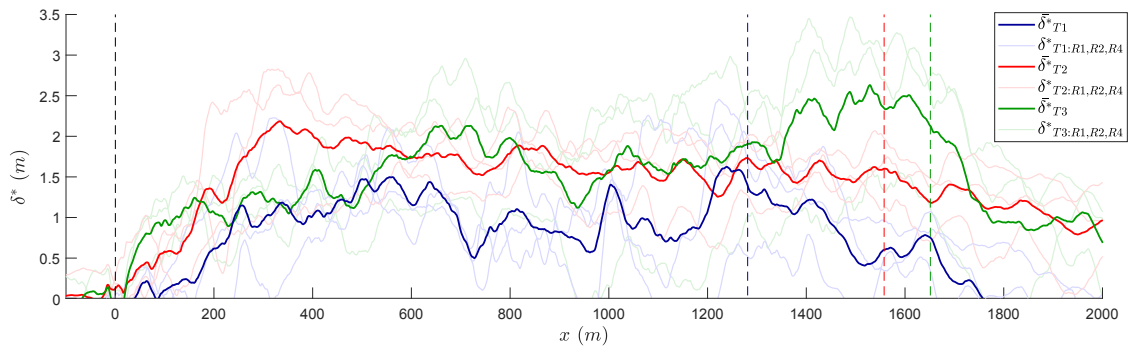


Figure 10: Displacement thickness,  $\delta^*$ , profiles for each train (T1,T2,T3) with relatively low crosswinds ( $\beta < 2^\circ$ ). An ensemble average, as well as individual rake profiles are presented for each train. Dotted lines indicate the location of the train noses and respective tails.

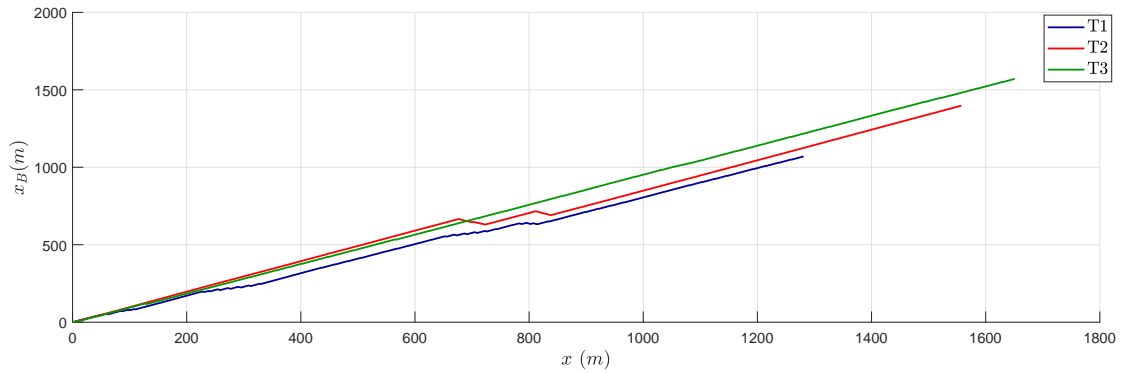


Figure 11: Cumulative blockage profiles of trains T1, T2 & T3.

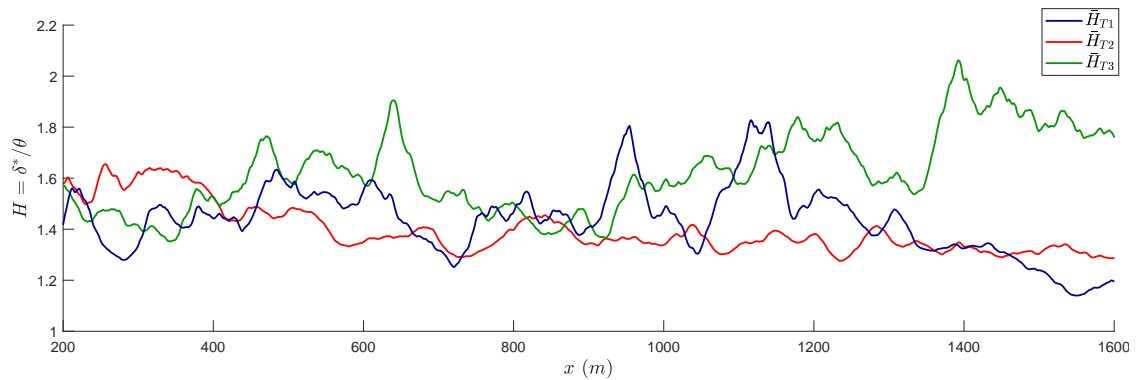


Figure 12: Shape factor,  $H$ , profiles of trains T1, T2 & T3.

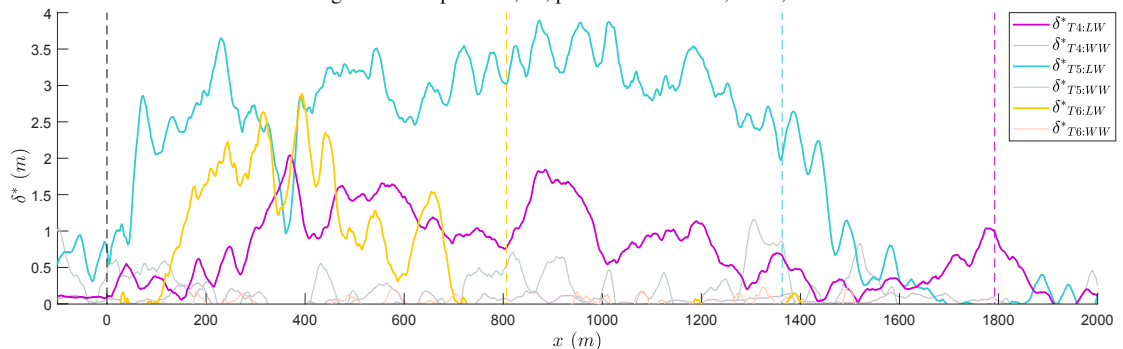


Figure 13: Displacement thickness,  $\delta^*$ , profiles for each train (T4,T5,T6) with relatively high crosswinds ( $\beta > 2^\circ$ ). An ensemble average, as well as individual rake profiles are presented for each train. Dotted lines indicate the location of the train noses and respective tails.

355 *3.2.2. Turbulence characterisation*

356 The flow that the measurement probes are exposed to as the trains pass is statistically non-stationary.  
 357 Single events such as the nose/tail passing and unique gaps configurations, result in a flow that changes  
 358 over time, rather than fluctuates around a consistent mean (a statistically stationary flow). Thus, the typical  
 359 description of turbulence, quantified by turbulence intensity:

$$I_u = \frac{\sigma_u}{(u_t - \bar{u})}, \quad I_v = \frac{\sigma_v}{(u_t - \bar{u})}, \quad I_w = \frac{\sigma_w}{(u_t - \bar{u})}, \quad (6)$$

360 where  $\sigma_{u,v,w}$  and  $\bar{u}$  are calculated over an entire statistically stationary signal, is not applicable here.

361 In order to provide an indication of the turbulence within the boundary layer of full-scale freight trains,  
 362 turbulence intensity along the train length is calculated over a moving window of filtered data. A single-  
 363 pole Butterworth, 0.03–100 Hz band-pass filter was applied to the velocity measurements. The cut-off  
 364 limits correspond respectively to a spatial length of less than the train lengths (0.03 Hz corresponds to  
 365  $\approx 1000$  m), and of the upper limit of the measurement system's frequency response. In Figure 14, the  
 366 effect of the filtering of an example velocity time-series is illustrated, with the filtered result resembling a  
 367 stationary signal. Regardless, a 5 s moving window was used to calculate the turbulence intensity over the  
 368 length of the train:

$$I_u(x) = \frac{\sigma_u(x)}{(u_t - \bar{u}(x))}, \quad I_v(x) = \frac{\sigma_v(x)}{(u_t - \bar{u}(x))}, \quad I_w(x) = \frac{\sigma_w(x)}{(u_t - \bar{u}(x))}, \quad (7)$$

369 where  $\sigma_{u,v,w}(x)$  and  $\bar{u}(x)$  are calculated over a moving window equivalent to five seconds ( $x \approx 150m$ )  
 370 along the train length.

371 The longitudinal turbulence intensity,  $I_u(x)$ , calculated using equation 7, measured by each of the 7  
 372 probes in the horizontal rake, R1, for train T3, is shown in Figure 15. These results are again representative  
 373 of the trains [T1, T2, T3] measured with low crosswind;  $u_a < 4$  m/s (relative yaw angle,  $\beta < 2^\circ$ ).  
 374 Turbulence intensities of 10–30% were measured, highest closest to the train, that increases along the length  
 375 as the boundary layer thickness increases. These levels of turbulence are similar to the analogous case of  
 376 on-road turbulence – what an automotive vehicle (of similar velocity and scale as shipping containers)  
 377 experiences when operating on the road, including the effect of the environment and other vehicles –  
 378 characterised by Wordley and Saunders (2008) and McAuliffe et al. (2014) who found turbulence intensities  
 379 of  $I_u = 2$ –16%. In spite of the 5 second moving window over which the turbulence was calculated over,  
 380 the profiles show significant fluctuation in turbulence along the length. This demonstrates specific loading  
 381 configurations or local wind events (for example at  $x = 800$  m), can have a significant impact on the

382 boundary layer characteristics beyond the velocity profile.

383 In Figure 16, the different components of turbulence intensity,  $I_u$ ,  $I_v$ ,  $I_w$ , are presented for probe  
384 P1, in rake R1, for train T3. The anisotropic characteristics of the turbulence are relatively consistent:  
385  $I_u : I_v : I_w \approx 1 : 0.4 : 0.6$ , as the turbulence generally increases, with additional fluctuations along the  
386 train length. Interestingly, greater turbulence exists in the vertical direction than the horizontal. This is  
387 contrary to that generally found on roads by Wordley and Saunders (2008), who determined anisotropic  
388 ratios of  $I_u : I_v : I_w \approx 1 : 1 : 0.6$ , where the proximity to the ground is expected to reduce the level of  
389 velocity fluctuations. A potential explanation for this difference is that in these experiments, measurements  
390 were made specifically next to the vehicle, in contrast to general exposure to the effects of a number of  
391 vehicles and infrastructure characterised on-road.

392 The turbulence intensities,  $I_u$  and  $I_{u,v,w}$ , calculated using equation 6 over the middle 40% of the train,  
393 are presented on the vertical axis as points in their respective colours for all probes in Figure 15. This shows  
394 the different components of the closest probe in Figure 16, respectively. The middle 40% was calculated  
395 as the section of train where  $x = 0.3L_t : 0.7L_t$ , where  $L_t$  is the length of each train and was selected to  
396 exclude the effect of the nose and tail flow regions, to best represent a representative, if somewhat arbitrary,  
397 middle section of a freight train.

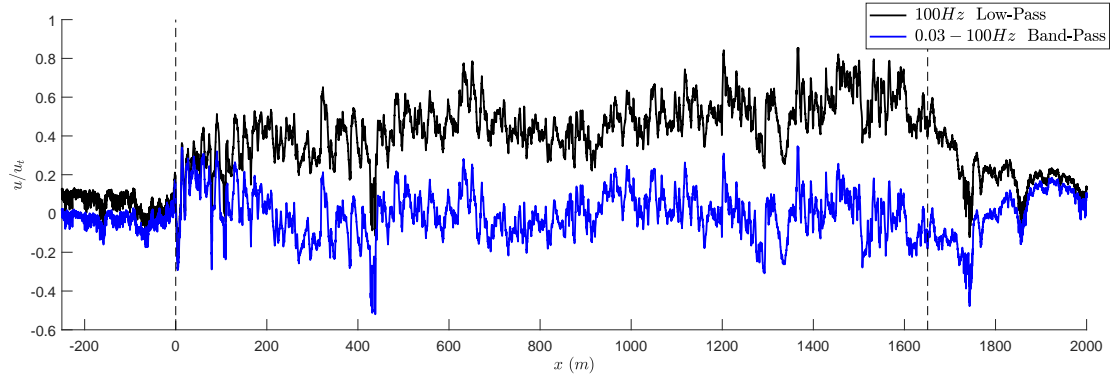


Figure 14: Normalised longitudinal velocity of P1, T1 with a 100 Hz low-pass and 0.03–100 Hz band-pass single-pole Butterworth filter applied, used to calculate turbulence intensity.

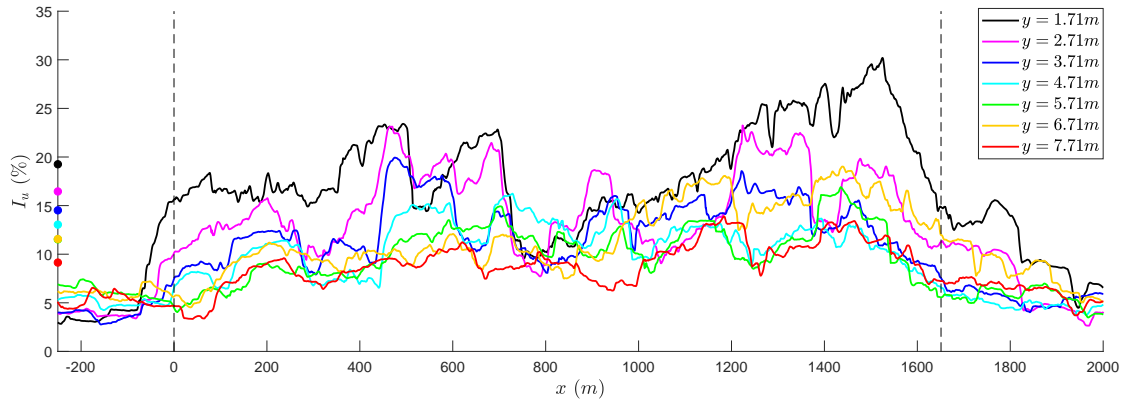


Figure 15: Longitudinal turbulence intensity  $I_u$  profile along the train T3, calculated over a 5 s moving window at each probe in rake R1. Average of the middle 40% of the train presented as corresponding coloured points on the vertical axis.

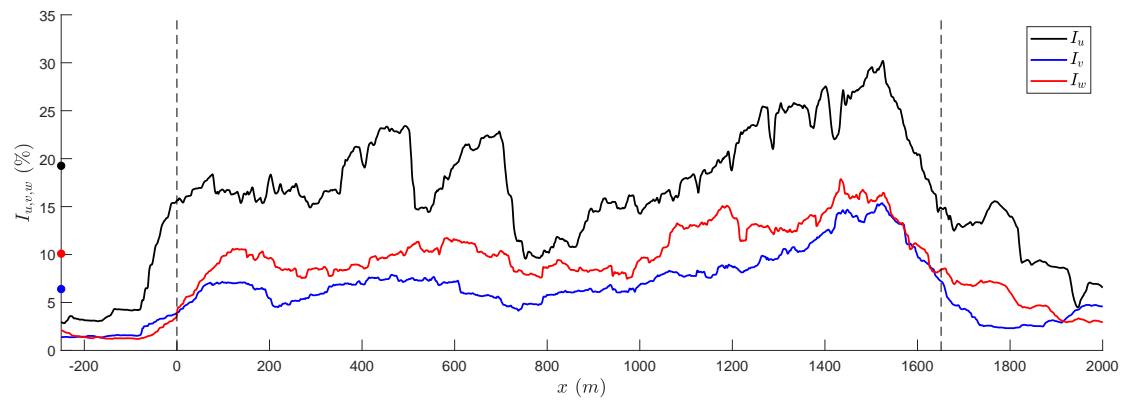


Figure 16: Profiles of the different components of turbulence intensity  $I_u, I_v, I_w$  along train T3, at probe P1, in rake R1. Average of the middle 40% of the train presented as corresponding coloured points on the vertical axis.

398 3.2.3. *Characteristic boundary layer*

399 The boundary-layer characteristics measured by all three horizontal rakes (R1, R2, R3) for the middle  
400 40% section of the three trains measured with low crosswind (T1, T2, T3) ( $u_a < 4$  m/s, relative yaw angle  
401  $\beta < 2^\circ$ ) have been averaged and are presented graphically in Figure 17 and tabulated in Table 2. These  
402 results are intended to be a reference for future investigations intending to model (or compare to) realistic  
403 boundary-layer characteristics experienced by an intermodel freight train. The corresponding standard  
404 deviation of each of the average characteristics are also presented at the bottom of Table 2 to provide an  
405 indication of the variability from the different rakes and trains measured.

406 The velocity, turbulence intensity and length-scale profiles of the characteristic boundary-layer are  
407 presented in Figure 17(a), (b) and (c), respectively. Included in Figure 17a, are the displacement thickness  
408 ( $\delta^*$ ) and momentum thickness ( $\theta$ ), based on the calculated average velocity profile. The boundary layer  
409 thickness ( $\delta_{99}$ ) was estimated from where  $u \approx 99\%$  of the ‘freestream’ velocity, from a simple power-law  
410 model of the velocity profile:

$$u = u_{ref} \left( \frac{y}{y_{ref}} \right)^\alpha, \quad (8)$$

411 where  $\alpha = 0.25$  and  $u_{ref}$  was the measured velocity at  $y_{ref} = 1.71$  m . These values are also provided in  
412 Table 3.

413 The anisotropic characteristics of the turbulence identified above for train T3, are the same in this  
414 characteristic boundary layer;  $I_u : I_v : I_w \approx 1 : 0.4 : 0.6$ , and remain consistent across the boundary layer  
415 thickness.

416 The length scales presented in Figure 17(c) were estimated by least-squares fitting of the Kármán  
417 spectra to the velocity measurements with the same single-pole Butterworth, 0.03–100 Hz band-pass filter  
418 described above, for the middle 40% section of each train. These results are again similar to on-road  
419 turbulence length scales of  $L_{u,v,w} = 2\text{--}10$  m (Wordley and Saunders, 2008, McAuliffe et al., 2014).

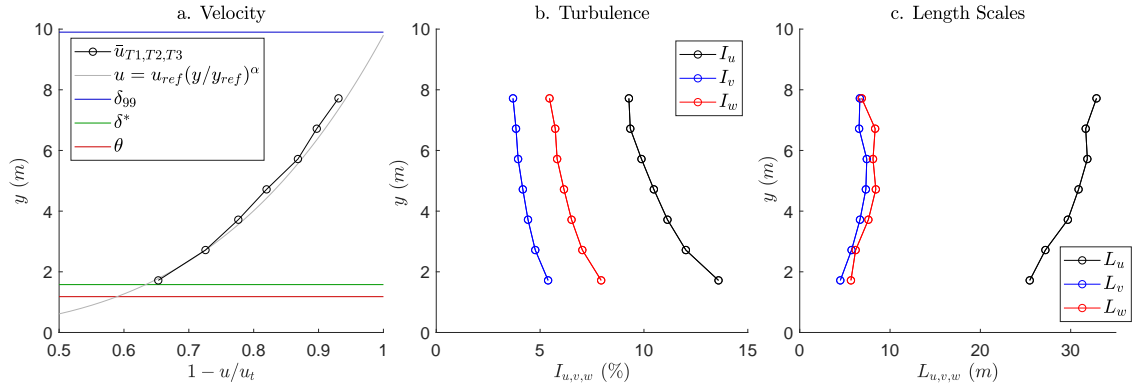


Figure 17: Characteristic boundary-layer properties: (a) Velocity (mean velocity, estimated boundary layer thickness, displacement thickness and momentum thickness), (b) turbulence, and (c) length-scale profiles.

Table 2: Characteristic boundary-layer properties for the low crosswind cases (T1, T2, T3).

$y$ (m)	$1 - u/u_t$	$I_u$ (%)	$I_v$ (%)	$I_w$ (%)	$L_u$ (m)	$L_v$ (m)	$L_w$ (m)
1.71	0.65	13.6	5.4	7.9	25.4	4.5	5.7
2.71	0.72	12.0	4.8	7.0	27.2	5.7	6.2
3.71	0.77	11.1	4.4	6.5	29.7	6.7	7.6
4.71	0.81	10.5	4.1	6.1	30.9	7.3	8.4
5.71	0.87	9.9	3.9	5.8	31.8	7.4	8.1
6.71	0.89	9.3	3.9	5.7	31.7	6.6	8.4
7.71	0.93	9.3	3.7	5.5	32.8	6.6	6.9
$\sigma$	0.08	1.7	0.5	0.8	9.5	2.4	2.4

Table 3: Boundary layer thickness characteristics for the low crosswind cases (T1, T2, T3).

$\delta_{99}$ (m)	$\delta^*$ (m)	$\theta$ (m)	$H$
9.9	1.6	1.2	1.34

### 420 3.3. Flow topology

421 The flow topologies around each of the freight trains are presented in two-dimensional planes in this  
422 section, complimented by wool-tuft flow visualisations. The three components of velocity,  $u, v, w$ , measured  
423 simultaneously by each probe using rakes R1 and R2, and for all trains, are presented in Figures 18, 19, and  
424 20, respectively. Note that in these and subsequent 2D spatial figures, the  $x$  and  $y$  axes are not presented  
425 with a true 1:1 scaling, in order to more easily interpret the data. These results enable further insight into  
426 the cause of the development and significant fluctuations in boundary-layer thickness along the length of  
427 the trains, and difference between each side of each train.

#### 428 3.3.1. Global topology

429 Clearly visible in Figure 18 is the significant difference in the  $u$  velocity for the trains with low cross-  
430 wind (T1, T2, T3) to the trains experiencing higher crosswinds (T4, T5, T6). Even for the trains under low  
431 crosswind, the flow around the train is asymmetric, which is unlikely to be caused by the predominantly  
432 symmetric loading configurations. This is clearer for T2 and T3, where a thicker region of induced flow on  
433 the positive  $y$  side of the trains – consistent with the positive  $\beta \approx 2^\circ$  ambient wind for both trains. Here,  
434 the (albeit low-level) crosswind effectively pushes the boundary layer towards the train surface, reducing  
435 its thickness on the windward side and increasing the level of induced flow on the leeward side to a peak  
436 of  $0.6u_t$ . This is seen to a significantly greater extent for the high crosswind trains (T4, T5, T6), where the  
437 boundary layer is reduced beyond the measurement points on the windward side, and the induced velocities  
438 increase to a level of up to  $0.8u_t$  on the leeward side.

439 Regardless of the observable influence of the low-cross wind on the flow topology, trains T2 and T3 also  
440 show the growing of the boundary layer along the train length. In contrast, train T1 exhibits fluctuations  
441 between stages of development and significant reduction, with considerably greater symmetric flow. These  
442 trends are also visible in the boundary layer displacement thickness profiles in Figure 10, with T2 and T3  
443 developing to a larger displacement thickness. As noted in Table 1, and quantified in Figure 11, the loading  
444 configuration of T1 contained the larger and more consistent gaps. Therefore, the loading configuration  
445 can be attributed as the cause for reduced boundary layer size. The greater symmetry observable for T1  
446 is likely attributable to the lower crosswind ( $\beta = -0.3$ ). However, the smaller boundary layer caused  
447 by the loading configuration may also result in the flow field being less sensitive to crosswind that is less  
448 observable in these results.

449 Inspection of the horizontal velocity component,  $v$ , in Figure 19 identifies the initial flow away from  
450 the head of the train ( $x = 0m$ ). The flow then generally tends towards the train surface with a magnitude of  
451  $v \approx 0.08u_t$ , with relatively incoherent oscillations along the trains. Stronger horizontal flow ( $v \approx 0.1u_t$ )

452 towards the rail centre occurs after the tail has passed as the wake closes. This is most clearly visible for  
453 train T2 in Figure 19b, and highlighted specifically with  $u, v$  velocity vectors presented in Figure 23.

### 454 3.3.2. Local topology

455 An apparent correlation is evident between the fluctuations in  $u$  and  $v$  velocity beyond the effect of  
456 crosswind already described. This occurs most clearly at  $x = 400$  m and  $x = 800$  m for train T1, where on  
457 the positive  $y$  side of the train, a large region of flow with an increase in  $v$  velocity directed towards the train,  
458 corresponds to a decrease in  $u$  velocity. The  $u$  velocity in the region over  $x = 400$ – $800$  m is presented in  
459 Figure 21 and  $u, v$  vectors over  $x = 600$ – $700$  m in Figure 22, with the loading configuration also illustrated  
460 from the light-gate measurements. In Figures 21 and 23, the turbulent flow field is visualised, with some  
461 indications of vortex structures existing in the flow arising from the shear layer interaction between the  
462 high velocity induced flow near the train surface and the ambient wind away from the train. However, from  
463 these results, a single gap on its own does not have a singular identifiable effect on the flow. It appears that  
464 it is the cumulative combination of a series of gaps that results in flow that is analogous to that seen at the  
465 tail of the train (Figure 23) and the overall decrease in the bulk induced flow.

466 The vertical velocity component,  $w$ , presented in Figure 20 shows regions of fluctuating sign at much  
467 smaller scales ( $\approx 10$ – $25$  m) than the fluctuations in longitudinal,  $u$  velocity ( $> 100$  m). This is evident  
468 most clearly for train T3, but also for trains T1, T2 and T4 on the leeward side. These fluctuations are  
469 strongest ( $w = \pm 0.1u_t$ ) closest to the surface, and convect away, lagging behind the point of origin. A  
470 possible explanation for such vertical velocity fluctuations and approximate length scales is the formation  
471 of horseshoe-type vortices rolling up in front of individual shipping containers with enough of a gap at  
472 the front to experience relatively clean flow. Although interesting, these result do not appear to have a  
473 significant effect on the overall boundary layer development.

474 The horizontal,  $v$  (Figure 19), and vertical,  $w$  (Figure 20), velocity components are difficult to interpret  
475 for the trains with high-crosswind (T4,T5,T6). The leeward side is expected to exhibit a three-dimensional  
476 flow topology, primarily consisting of a semi-longitudinal vortex that develops from separation at the lee-  
477 ward upper edge (Hemida and Baker, 2010, Copley, 1987). The  $v$  and  $w$  velocity magnitude and direction  
478 measured by the probes in the horizontal array are therefore dependent on the relative height of the structure  
479 as it passes through the array. In addition, such a structure is likely unsteady itself, and further influenced  
480 by the unsteady crosswind and non-uniform loading configuration. Thus, the  $v$  and  $w$  velocity figures are  
481 inconsistent for the different trains with high crosswinds, and no clear trends or characteristic features are  
482 able to be determined.

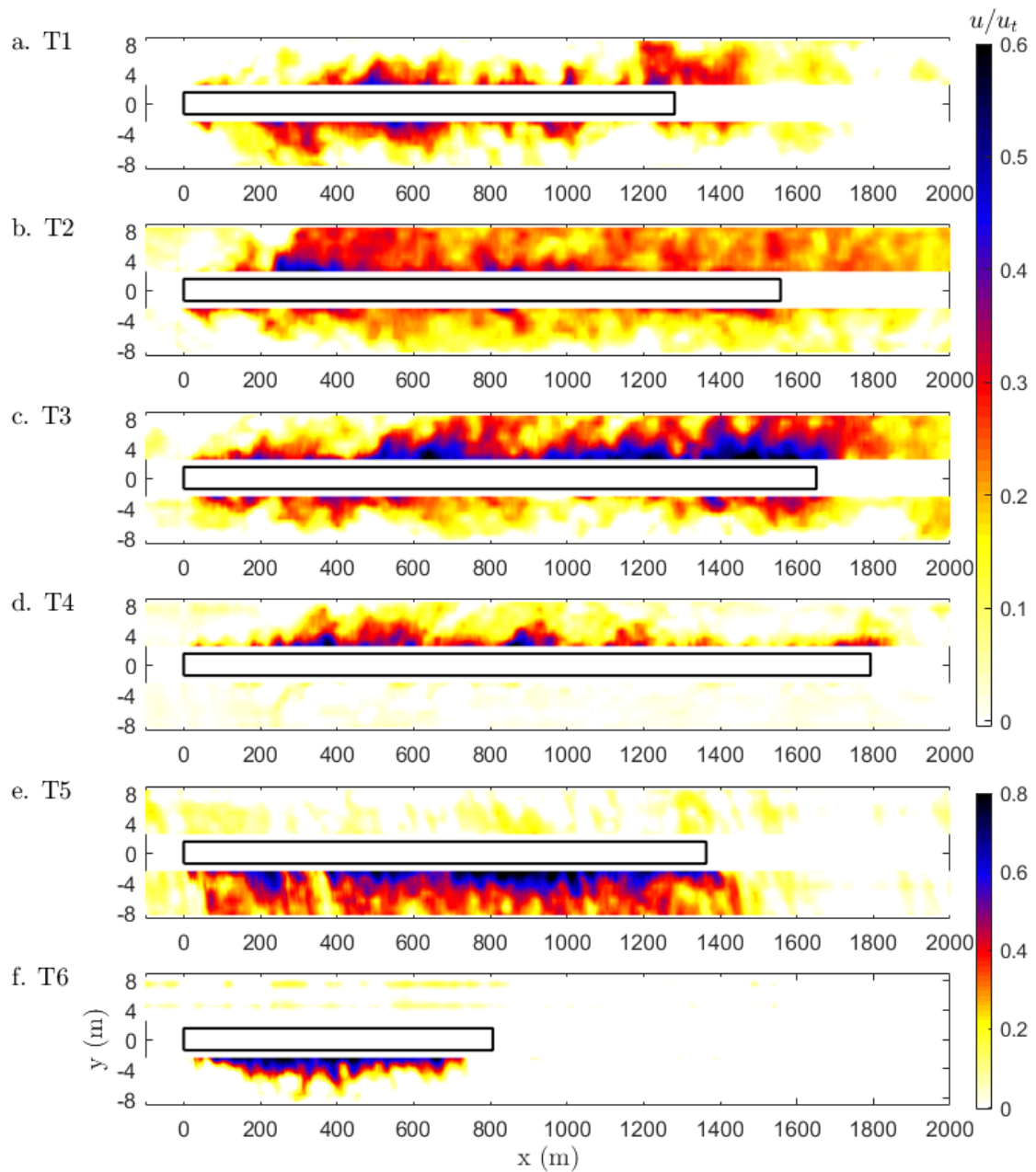


Figure 18: Coloured contours of longitudinal velocity,  $u/u_t$ , around trains T1–T6: (a)–(f). The position of each train indicated by a black outlined box.

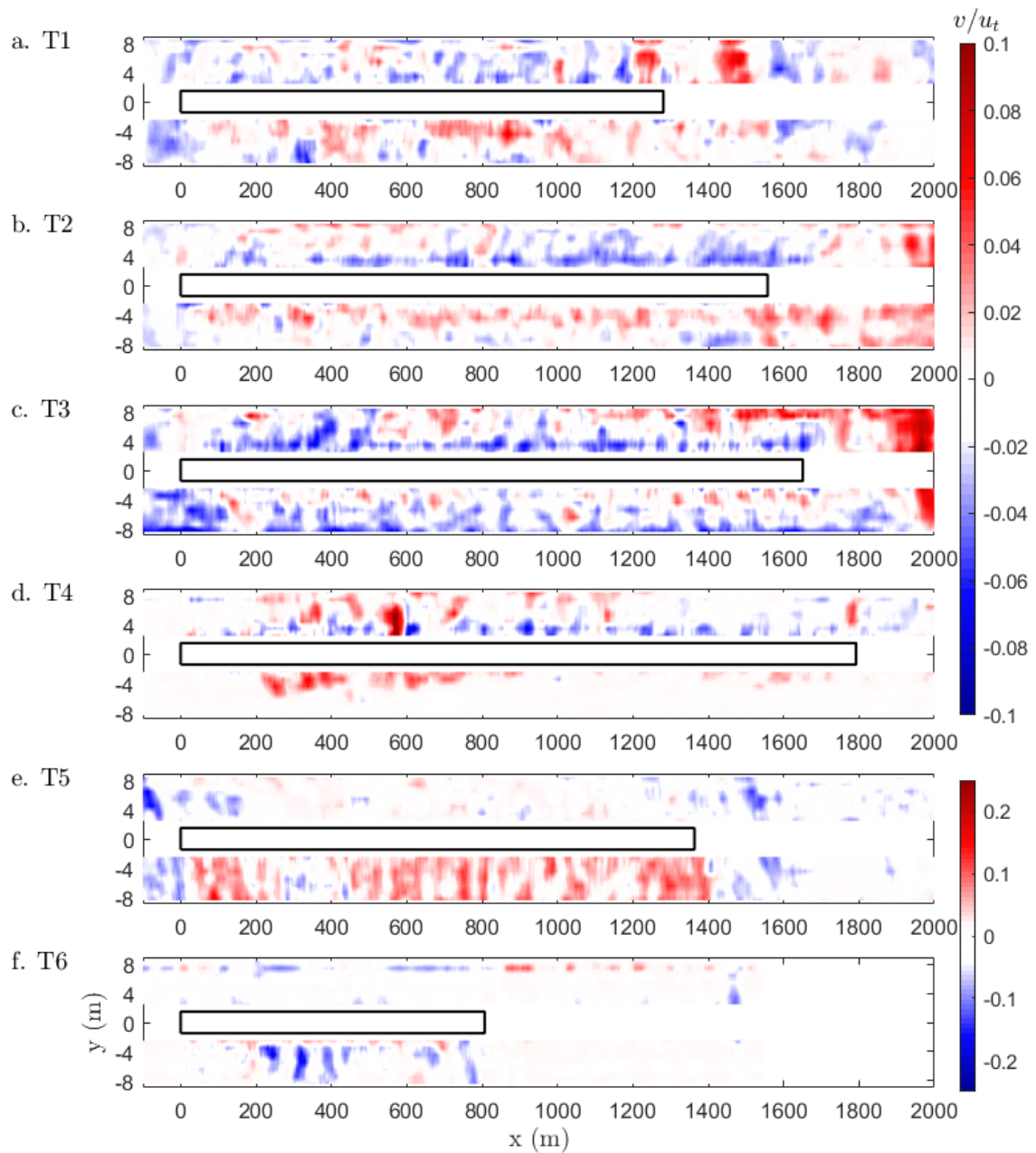


Figure 19: Coloured contours of horizontal velocity,  $v/u_t$ , around trains T1–T6: (a)–(f). The position of each train indicated by a black outlined box.

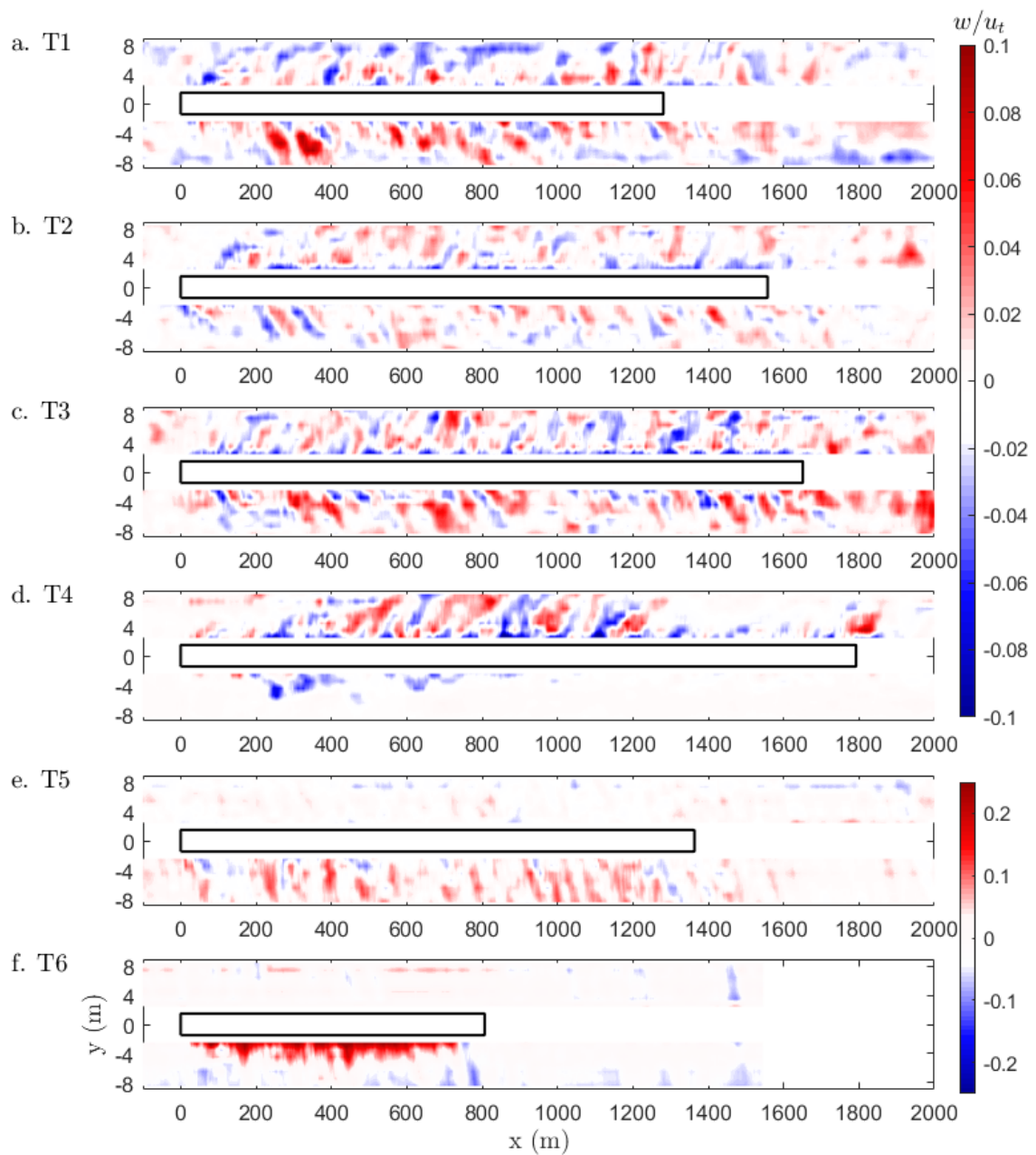


Figure 20: Coloured contours of vertical velocity,  $w/u_t$ , around trains T1–T6: (a)–(f). The position of each train indicated by a black outlined box.

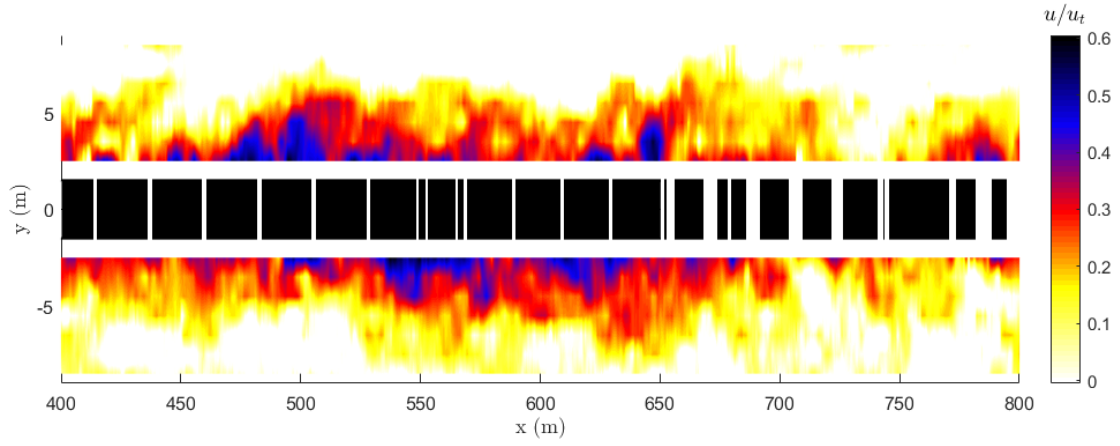


Figure 21: Coloured contours of longitudinal velocity,  $u/u_t$ , around train T1 over the section  $x = 400\text{--}800$  m with a series of consecutive gaps. Train indicated by black box and gaps by white spaces.

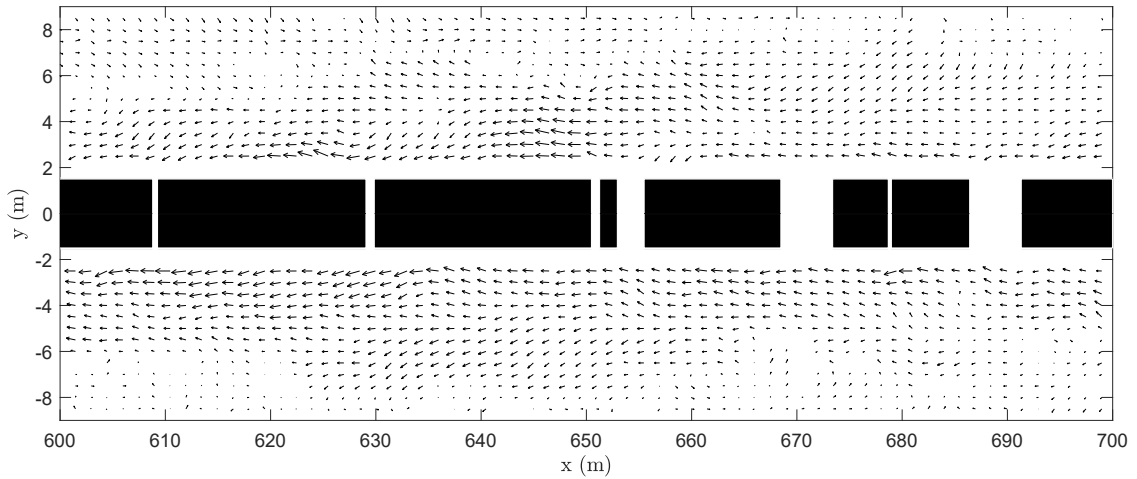


Figure 22: Velocity vectors of  $u, v$ , around train T1 over the section  $x = 600\text{--}700$  m with a series of consecutive gaps. Train indicated by black box and gaps by white spaces.

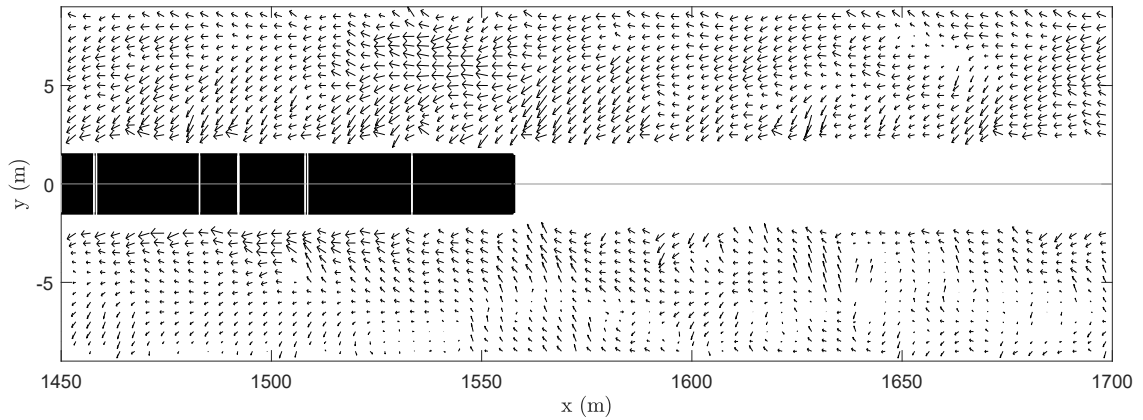


Figure 23: Velocity vectors of  $u, v$ , around train T1 over the section  $x = 1450\text{--}1700$  m, where the train tail is visible. Train indicated by black box and gaps by white spaces.

### 483 3.4. Frequency analysis

484 Frequency analysis was performed on the velocity measurements. In Figure 24, the frequency spectra  
485 from the seven probes in rake R1 calculated over the middle 40% of train T1 are presented for the different  
486 velocity components. The power spectral density was estimated using the Welch method with 8 Hamming  
487 windows and 50 % overlap. The results are representative of the low crosswind trains (T1, T2, T3).

488 A broad frequency band over the range of  $f = 0.5\text{--}5$  Hz with various specific peaks at  $f \approx 1, 1.5,$   
489  $2$  and  $3$  Hz are visible for all three velocity components. This band becomes stronger, closer to the train.  
490 Additional higher frequency peaks at  $f \approx 22$  Hz and  $f \approx 35$  Hz are also visible in the spectra across all of  
491 the measurement positions.

492 Due to the relative motion between the vehicle, the surrounding induced fluid flow and the measurement  
493 probe, it is difficult to separate periodic aerodynamic features (e.g. vortex shedding, as observed by Li et al.  
494 (2017) in the wake of containers) and periodic features caused by the train moving past the measurement  
495 equipment (e.g. repetitive passing of individual containers, ribs on the containers, wagons and bogies).

496 Vortex shedding from the sides of containers, if existent, would correspond to  $f \approx 3$  Hz (from an  
497 approximate Strouhal number of  $St_W \approx 0.2$  based on the container width). Higher frequency shear-layer  
498 vortices could also occur with  $f \approx 23$  Hz ( $St_W \approx 1.5$ ). Conversely, repetitive signals observed in the  
499 light gate measurements with length scales of 17–22 m associated to the wagons and/or containers passing  
500 the measurement position, correspond to frequencies of  $f \approx 1.4\text{--}1.75$  Hz. Repetitive signals from the  
501 container ribs ( $x \approx 0.2$  m) correspond to much higher frequencies of  $f \approx 150$  Hz. These values are based  
502 on the train speed of  $u_t = 30$  m/s. However, the boundary layer is also likely to modify the flow conditions  
503 such estimations are based on. This could result in a reduced effective velocity, and increased effective  
504 widths, and therefore different corresponding expected frequencies.

505 Although minor trends and features in the spectra can be observed, there are no clear dominant fre-  
506 quencies that can be directly attributable to unsteady aerodynamic characteristics. This can be expected for  
507 real-world measurements in complex conditions. Regardless of the difficulty in their interpretation, these  
508 results are presented as they may be useful for comparison to future wind-tunnel or numerical aerodynamic  
509 investigations of freight trains.

### 510 3.5. Correlation

511 Analysis of the cross-correlation of the velocity fluctuations between the probes at different positions  
512 provides insight into the existence and scale of coherent flow structures. Such analysis is also useful to  
513 infer the influence that the loading configuration has on the flow field, in contrast to the ambient wind.

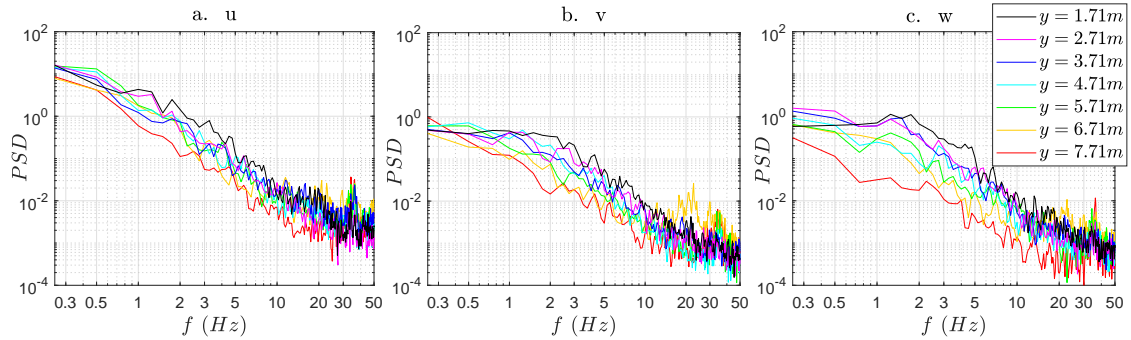


Figure 24: Power spectral density (PSD) determined from Fast Fourier Transform (FFT) of the different velocity components: (a)  $u$ , (b)  $v$ , (c)  $w$  measured by probes P1–P7 from rake R1, taken over the middle %40 section of train T1.

514 In this section, correlation analysis over the middle 40% section of train T1 is presented for the different  
 515 velocity components. The results are representative of the low crosswind trains (T1, T2, T3).

516 In Figure 25, the cross-correlation of probe P1 (closest to the train,  $y = 1.71$  m) with each of the  
 517 probes (P1–P7) in rake R1 is presented for the  $u$  velocity component. As expected, moving away from the  
 518 train, reducing correlation is visible. The correlation coefficient,  $\rho$ , decreases from a relatively high value  
 519 ( $\rho = 0.6$ ) over a short distance ( $\Delta y = 1$  m), to a relatively low value ( $\rho = 0.2$ ) at the largest distance  
 520 ( $\Delta y = 6$  m). Similarly, an increasing time-lag exists moving away from the train before the probes exhibit  
 521 their highest correlation. This time-lag is perhaps expected for the close probes (e.g.  $t < 1.7$  s for  $\Delta y < 4$   
 522 m), however, it increases significantly for  $\Delta y = 5$  m and  $\Delta y = 6$  m, to considerable time-lags of  $t \approx 5$   
 523 s and  $\approx 8$  s (corresponding to  $x \approx 240$  m) respectively. These findings are supported by the results in  
 524 Figure 18, where a fluctuation or feature in the velocity close to the train only convects to the furthest  
 525 measurement position after a longitudinal length in the range of  $x \approx 240$  m.

526 Correlation in the transient flow field either side of the train would indicate the loading configuration  
 527 has a significant effect on the flow field, as its influence is expected to be symmetric, affecting both sides  
 528 at the same time. In contrast, cross-wind is expected to reduce symmetric in-phase correlation. Symmetric  
 529 horizontal correlation was investigated by calculating the cross-correlation between the respective probes  
 530 in rakes R1 and R2 on either side of the train (e.g. R1, P1 ( $y = 1.71$  m) to R2, P1 ( $y = -1.71$  m)). The  
 531 results for the  $u$  velocity component are presented in Figure 26. The probes close to the train ( $y = 1.71$ ,  
 532  $2.71$ ,  $3.71$  m) exhibit reasonably high correlation with each other ( $\rho \approx 0.4$ ). However, the two probes at  
 533  $y = 2.71$  and  $3.71$  m exhibit the highest correlation for a time-lag of  $\pm 1$  s, indicating that already at these  
 534 distances, the ambient crosswind may be skewing the flow. Negligible correlation was apparent for the  $v$   
 535 and  $w$  velocity components for either the symmetric or one-sided horizontal correlation analysis.

536 Longitudinal correlation was analysed using the measurements made at the different rakes (R1, R3,

537 R4) on the same side (+ $y$ ) of the train. This enabled two cases with  $\Delta x = 15$  m (R1–R2, R3–R4) and one  
 538 case of  $\Delta x = 30$  m (R1–R4) to be analysed. The autocorrelation of R1 probes with themselves were also  
 539 calculated, and all cases are presented in Figure 27 for the four horizontal probe positions closest to the  
 540 train. The  $u$  component of velocity is only presented here, as the  $v$  and  $w$  components exhibited negligible  
 541 correlation.

542 If the flow field around the train were steady over time, high levels of correlation would exist with  
 543 time-lags corresponding to their distances relative to each other at the test-site divided by the train velocity  
 544 ( $t = \Delta x/u_t = 0.5$  &  $1$  s when  $\Delta x = 15$  &  $30$  m, respectively). However, this is not observed in the  
 545 results. Distinct peaks in correlation coefficient of  $\rho \approx 0.4$  are visible for both longitudinal distances;  
 546 however, they are not consistent across the different horizontal positions. In spite of this inconsistency, a  
 547 trend is visible of increasing time-lag moving away from the train in the horizontal direction. Even at the  
 548 closest position,  $y = 1.71$  m, the time-lag of  $\approx 1$  s is greater than the estimated lag of  $0.5$  s using distance  
 549 and train speed. This increasing time-lag indicates that transient flow structures are generated at the train  
 550 and then convect away with reducing velocity. The remaining velocity fluctuations not contributing to the  
 551  $\rho \approx 0.4$  correlated flow could be attributed to additional transient features in the flow, as well as the effect  
 552 of transient crosswinds.

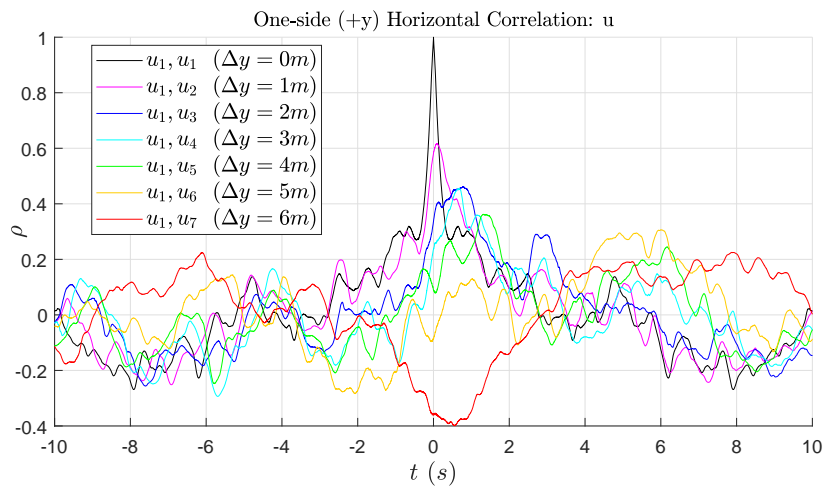


Figure 25: Cross correlation of the longitudinal velocity,  $u$ , measured over the middle 40% section of train T1 by each probe (P1–P7) in the horizontal rake R1, with P1, presented in terms of the correlation coefficient,  $\rho$ .

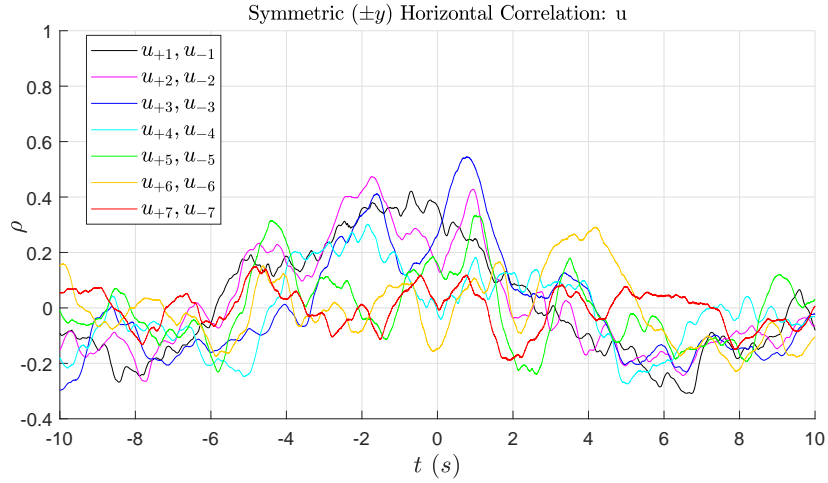


Figure 26: Cross correlation of the longitudinal velocity,  $u$ , measured over the middle 40% section of train T1 by each probe (P1-P7) in the horizontal rake R1 ( $+y$ ) to its corresponding probe (P1-P7) on the other side of the train in rake R2 ( $-y$ ).

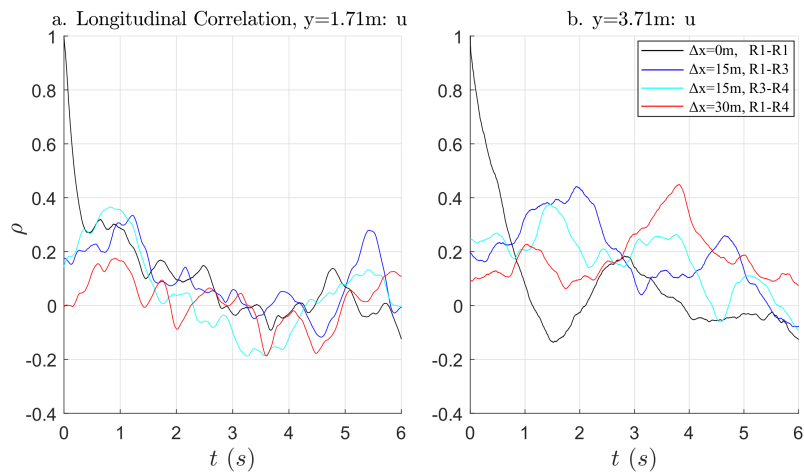


Figure 27: Cross correlation of the longitudinal velocity,  $u$ , measured over the middle 40% section of train T1 over different longitudinal distances:  $\Delta x = 0m$  (R1-R1),  $\Delta x = 15m$  (R1-R3, R3-R4),  $\Delta x = 30m$  (R1-R4), from different corresponding probes. (a) P1 ( $y = 1.71 m$ ) and (b) P3 ( $y = 1.71 m$ ) in each of the different rakes: R1, R3, R4, on the same side of the train ( $+y$ ).

553 **4. Conclusions**

554 The boundary layers that develop on the sides of full-scale operational inter-model freight trains have  
 555 been measured at a test-site set-up situated around a single standard-gauge rail in Victoria, Australia. Rakes  
 556 of 4-hole dynamic-pressure probes were utilised to measure the velocity induced by passing trains, enabling  
 557 calculation of the boundary layer characteristics, as well as providing insight into the transient flow topol-  
 558 ogy around a set of six trains.

559 The *characteristic boundary layer* – an average boundary layer that occurs at the approximate middle  
 560 of freight trains operating within low ambient wind ( $\beta < 2^\circ$ ) – was determined to have: a displacement  
 561 thickness of  $\delta^* = 1.6$  m (within a range of  $\delta^* = 0.5\text{--}3$  m), a turbulence intensity profile ranging from 4–  
 562 13% with relatively consistent anisotropy ratios of  $I_u : I_v : I_w \approx 1 : 0.4 : 0.6$ , and turbulent length-scales  
 563 in the range 5–30 m. This characteristic boundary layer and its additional salient features are illustrated in  
 564 Figure 28; it is intended to help inform future experiments and simulations, in order to model real-world  
 conditions experienced by moving freight trains.

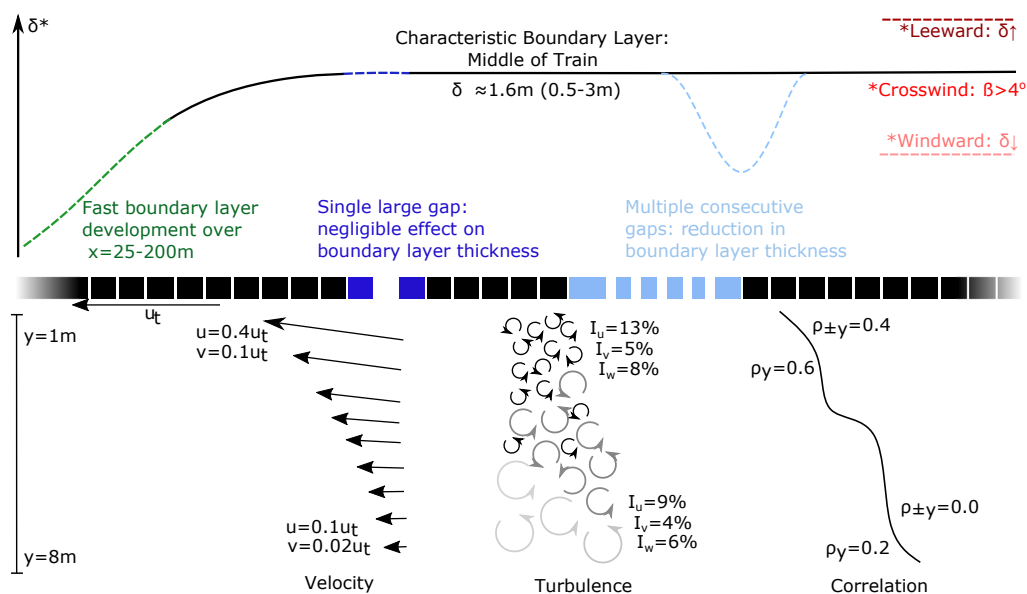


Figure 28: Salient features of the characteristic boundary layer around an operational inter-modal freight train.

565

566 Even relatively low ambient-wind conditions (with relative yaw angles  $\beta < 2^\circ$ ) were observed to have  
 567 an effect on the boundary layer and flow topology at the two sides of a train. Measurements taken either side  
 568 of the trains exhibited differences in the calculated displacement thickness – and corresponding agreement  
 569 for multiple measurements taken on the same side of the train - as well as visible asymmetry in the flow  
 570 topology. These results are not expected to be caused by the loading configuration of the vehicles, and thus  
 571 can be attributed to the (albeit weak) mean and fluctuating components of the ambient wind.

572 Loading configuration was found to only have a noticeable influence on the displacement thickness  
573 and flow topology when a series of consecutive gaps ( $> 2$  m) between shipping containers existed. This  
574 loading configuration led to a reduction in displacement thickness and the bulk induced flow around the  
575 train, as one would expect. A measure of the cumulative blockage of the trains was shown to be useful  
576 in visualising the loading configuration and exhibited the same trends in the large-scale variation of the  
577 displacement thickness profile along the freight trains. No single gap, in spite of significant sizes ( $> 10$  m),  
578 was observed to have an observable/measurable effect on either the flow field or displacement thickness,  
579 at least in the measurement region away from the train side surfaces. (The first probe was located at 1.7 m  
580 from the train of width 2.1 m).

581 The rakes of 7 probes either side of the train provided some insight into transient flow field around the  
582 train. Following rapid development of the boundary layer over the first 200 m, the average flow field at  
583 the middle of the trains exhibited longitudinal velocities of  $u = 0.4u_t$  (40% of the train speed) and flow  
584 towards the train surface of  $v = 0.1u_t$  at  $y = 1.71$  m from the surface, reducing to  $u = 0.1u_t$  &  $v = 0.02u_t$   
585 respectively at  $y = 7.71$  m away from the surface. Fluctuations in longitudinal velocity, caused by large-  
586 scale turbulent structures were observed to convect away with reducing velocity from the train surface  
587 and downstream. This was evident in the velocity coloured contours and identified in the horizontal and  
588 longitudinal correlation analysis. Further, the transient flow was seen to be somewhat correlated either side  
589 of the train, with maximum correlation coefficients of  $\rho = 0.4$  recorded closest to the train ( $\pm y = 1.71$  m)  
590 reducing to  $\rho = 0$  away from the train ( $\pm y = 7.71$  m). This symmetric horizontal correlation is expected to  
591 be caused by the loading configuration influencing the flow topology. Frequency analysis was performed,  
592 however clear dominant frequencies were not evident, with the results being difficult to interpret due to the  
593 relative motion of the experiment.

594 Higher crosswinds ( $\beta = 4\text{--}10^\circ$ ) resulted in the flow field on the windward side of the train being pushed  
595 close to the surface beyond the reach of the measurement equipment. On the leeward side of the train, signs  
596 of the three-dimensional flow field consisting of system of longitudinal vortices forming from separation at  
597 the trailing edges of the train and containers were observed, but it was not possible to clearly characterise  
598 these due to their complexity and lack of measurement resolution. This resulted in significantly larger  
599 bulk induced flow on the leeward side of the train with larger velocities than observed in low crosswind  
600 conditions.

601 The findings presented from this novel experiment: characterising and quantifying the boundary layer  
602 structure, and providing insight into the transient flow topology around freight trains, together provide  
603 aerodynamic characteristics of typical inter-modal freight trains operating in open air under low crosswind

604 conditions.

605 The sample size of six trains is acknowledged to be relatively small, even considering that each train  
606 is effectively measured three times by each of the horizontal boundary-layer rakes. However, these are the  
607 first measurements attempting to spatially and temporally resolve the boundary layers of freight trains op-  
608 erating in real-world conditions. The corresponding results provide (even with variation between different  
609 trains as well as along each train's length) an indication of boundary-layer characteristics representative of  
610 real-world freight trains that are significantly different than what is typically modelled in wind-tunnel and  
611 numerical simulations. These results provide valuable insight that can be useful for comparative aerody-  
612 namic investigations on inter-modal freight train aerodynamics in the future.

## 613 **5. Acknowledgements**

614 This research was supported through Pacific National Rail, specifically Michael Kost and Tony Mc-  
615 Greevy, and the Australian Research Council's Linkage Project funding scheme, under project number  
616 LP13100953. The Australian Rail Track Corporation, notably Sean Adams, are acknowledged for en-  
617 abling access to the rail corridor. Track force protection services were provided by Paul Jerman from Rail  
618 Operations Consulting and Lindsay Hauesler from Aspect Rail. Support from the Monash Wind Tunnel  
619 Platform technical staff is acknowledged, specifically Senior Technical Officer Greg Hewes for his extraor-  
620 dinary contribution to the development of the experimental setup, and undertaking of the measurements in  
621 challenging conditions.

## 622 **References**

### 623 **References**

- 624 Baker, C. (2010), 'The flow around high speed trains', *Journal of Wind Engineering and Industrial Aerodynamics* **98**, 277–298.
- 625 Beagles, A. and Fletcher, D. (2013), 'The aerodynamics of freight: approaches to save fuel by optimising the utilisation of container  
626 trains', *Proc IMechE Part F: J Rail and Rapid Transit* **227(6)**, 635–643.
- 627 Bell, J., Burton, D., Thompson, M., Herbst, A. and Sheridan, J. (2015), 'Moving model analysis of the slipstream and wake of a  
628 high-speed train', *Journal of Wind Engineering and Industrial Aerodynamics* **136**, 127–137.
- 629 Bell, J., Burton, D., Thompson, M., Herbst, A. and Sheridan, J. (2016a), 'Dynamics of trailing vortices in the wake of a generic  
630 high-speed train', *Journal of Fluids and Structures* **65**, 238–256.
- 631 Bell, J., Burton, D., Thompson, M., Herbst, A. and Sheridan, J. (2016b), 'Flow topology and unsteady features in the wake of a  
632 generic high-speed train', *Journal of Fluids and Structures* **61**, 168–183.
- 633 Bell, J., Burton, D., Thompson, M., Herbst, A. and Sheridan, J. (2017), 'A wind-tunnel methodology for assessing the slipstream of  
634 high-speed trains', *Journal of Wind Engineering and Industrial Aerodynamics* **166**, 1–19.

635 Bell, J., Burton, D., Thompson, M., Herbst, A. and Sheridan, J. (8-11 December, 2014), 'The effect of length to height ratio on the  
636 wake structure and surface pressure of a high-speed train', *19th Australasian Fluid Mechanics Conference (AMFC), Melbourne,*  
637 *Australia* .

638 Bergh, H. and Tijdeman, H. (1965), 'Theoretical and experimental results for the dynamic response of pressure measuring systems',  
639 *National Aero and Astronautical Research Institute, Amsterdam* **328**(Report NLR-TRF).

640 Buhr, A. and Ehrenfried, K. (2017), 'High-speed particle image velocimetry of the flow around a moving train model with boundary  
641 layer control elements', *International Journal of Mechanical, Aerospace, Industrial, Mechatronic and Manufacturing Engineering*  
642 **11**(3), 47–55.

643 CEN (2013), 'European Committee for Standardization. Railway Applications - Aerodynamics — Part 4: Requirements and test  
644 procedures for aerodynamics on open track, CEN EN 14067-4'.

645 Cooper, K. and Campbell, W. (1981), 'An examination of the effects of wind turbulence on the aerodynamic drag of vehicles', *Journal*  
646 *of Wind Engineering and Industrial Aerodynamics* **9**, 167–180.

647 Copley, J. (1987), 'The 3-d flow around railway trains', *Journal of Wind Engineering and Industrial Aerodynamics* **26**.

648 Engdahl, R., Gielow, R. and Paul, J. (1986), 'Train resistance - aerodynamics volume i of ii intermodal car application', *Proceedings*  
649 *of Railroad Energy Technology Conference II. Association of American Railroad, Atlanta, GA.* pp. 225–268.

650 Flynn, D., Hemida, H. and Baker, C. (2016), 'On the effect of crosswinds on the slipstream of a freight train and associated effects',  
651 *Journal of Wind Engineering and Industrial Aerodynamics* **156**, 14–28.

652 Flynn, D., Hemida, H., Soper, D. and Baker, C. (2014), 'Detached-eddy simulation of the slipstream of an operational freight train',  
653 *Journal of Wind Engineering and Industrial Aerodynamics* **132**, 1–12.

654 Gallagher, M., Morden, J., Baker, C., Soper, D., Quinn, A., Hemida, H. and Sterling, M. (2018), 'Trains in crosswinds - compari-  
655 son of full-scale on-train measurements, physical model tests and cfd calculations', *Journal of Wind Engineering and Industrial*  
656 *Aerodynamics* **175**, 428–444.

657 Gielow, M. and Furlong, C. (1988), 'Results of wind tunnel and full-scale tests conducted from 1983 to 1987 in support of the  
658 association of american railroads' train energy program', *Publication R-685 Association of American Railroads* .

659 Hemida, H. and Baker, C. (2010), 'Large-eddy simulation of the flow around a freight wagon subjected to a crosswind', *Computers*  
660 *& Fluids* **39**, 1944–1956.

661 Holmes, J. (2001), *Wind loading of structures*, Spon Press, New York.

662 Iberall, A. (1950), 'Attenuation of oscillatory pressures in instrument lines', *US Department of Commerce National Bureau of Standards*  
663 **45**(RP2115), 93–107.

664 Irwin, H. (1981), 'The design of spires for wind simulation', *Journal of Wind Engineering and Industrial Aerodynamics* **7**, 361–366.

665 Irwin, H., Cooper, K. and Girard, R. (1979), 'Correction of distortion effects caused by tubing systems in measurements of fluctuating  
666 pressures', *Journal of Industrial Aerodynamics* **5**, 93–107.

667 Lai, Y.-C. and Barkan, C. (2005), 'A rolling horizon model to optimize aerodynamic efficiency of intermodal freight trains with  
668 uncertainty', *Transportation Research Record: Journal of the Transportation Research Board* **1916**, 47–55.

669 Lai, Y.-C., Ouyang, Y. and Barkan, C. (2008), 'A rolling horizon model to optimize aerodynamic efficiency of intermodal freight  
670 trains with uncertainty', *Transportation Science* **42**(4), 466–477.

671 Li, C., Burton, D., Kost, M., Sheridan, J. and Thompson, M. (2017), 'Flow topology of a container train wagon submitted to varying  
672 local loading configurations', *Journal of Wind Engineering and Industrial Aerodynamics* **169**, 12–29.

673 Lukaszewicz, P. (2007), 'A simple method to determine train running resistance from full-scale measurements', *Proc IMechE Part F:*  
674 *J Rail and Rapid Transit* **221**, 331–338.

675 Lukaszewicz, P. (2009), 'A simple method to determine train running resistance from full-scale measurements', *Proc IMechE Part F:*

676 *J Rail and Rapid Transit* **223**, 189–197.

677 Maleki, S., Burton, D. and Thompson, M. (2017), ‘Assessment of various turbulence models (eles, sas, urans and rans) for predicting  
678 the aerodynamics of freight train container wagons’, *Journal of Wind Engineering and Industrial Aerodynamics* **170**, 68–80.

679 Maleki, S., Burton, D. and Thompson, M. (2019), ‘Flow structure between freight train containers with implications for aerodynamic  
680 drag’, *Journal of Wind Engineering and Industrial Aerodynamics* **188**, 194–206.

681 McAuliffe, B., Belluz, L. and Belzile, M. (2014), ‘Measurement of the on-road turbulence environment experienced by heavy duty  
682 vehicles’, *SAE Int. J. Commer. Veh.* **7(2)**.

683 Muld, T., Efraimsson, G. and Hennigson, D. (2013), ‘Wake characteristics of high-speed trains with different lengths’, *Proc. IMechE*  
684 *Part F: Journal of Rail and Rapid Transport* **228(4)**, 333–342.

685 ■ Öngüner et al.

686 Öngüner, E., Henning, A., Fey, U. and Wagner, C. (2020), ‘Towards aerodynamically optimized freight wagons: An experimental  
687 study on container designs’, In: *Dillmann A., Heller G., Krämer E., Wagner C., Tropea C., Jakirlić S. (eds) New Results in*  
688 *Numerical and Experimental Fluid Mechanics XII. DGLR 2018. Notes on Numerical Fluid Mechanics and Multidisciplinary*  
689 *Design* **142**, 437–446.

690 Östh, J. and Krajnović, S. (2014), ‘A study of the aerodynamics of a generic container freight wagon using large-eddy simulation’,  
691 *Journal of Fluids and Structures* **44**, 31–54.

692 Paul, J., Johnson, R. and Yates, R. (2007), ‘Application of cfd to rail car and locomotive aerodynamics’, *The Aerodynamics of Heavy*  
693 *Vehicles II: Trucks, Buses and Trains* pp. 259–297.

694 Peters, J. (1993), ‘Effect of reynolds number on the aerodynamic forces on a container model’, *Journal of Wind Engineering and*  
695 *Industrial Aerodynamics* **49**, 431–438.

696 Raghunathan, R., Kim, H. and Setoguchi, T. (2002), ‘Aerodynamics of high-speed railway train’, *Progress in Aerospace Sciences*  
697 **38**, 469–514.

698 Shetz, J. (2001), ‘Aerodynamics of high-speed trains’, *Annual Review of Fluid Mechanics* **33**, 371–414.

699 Sima, M., Tietze, A., Schulz, B. and Ehrenfried, K. (2016), ‘Representing large boundary layers in slipstream moving model tests’,  
700 *Railways 2016, The thirds international conference on railway technology: research development and maintenance, 05-07 April,*  
701 *Cagliari, Italy.*

702 Sims-Williams, D. (2011), ‘Cross winds and transients: reality, simulation and effects’, *SAE Technical Paper* **01-0172**.

703 Soper, D. (2014), ‘The aerodynamics of a container freight train’, *PhD Thesis, University of Birmingham*.

704 Soper, D. and Baker, C. (2019), ‘A full-scale experimental investigation of passenger and freight train aerodynamics’, *Proc IMechE*  
705 *Part F: J Rail and Rapid Transit* **0(0)**, 1–16.

706 Soper, D., Baker, C. and Sterling, M. (2014), ‘Experimental investigation of the slipstream development around a container freight  
707 train using a moving model facility’, *Journal of Wind Engineering and Industrial Aerodynamics* **135**, 105–117.

708 Sterling, M., Baker, C., Jordan, S. and Johnson, T. (2008), ‘A study of the slipstreams of high-speed passenger trains and freight  
709 trains’, *Proc. Institute of Mechanical Engineers Part F: Journal of Rail and Rapid Transport* **222**, 177–193.

710 Storms, B., Salari, K. and Babb, A. (2008), ‘Fuel savings & aerodynamic drag reduction from rail car covers’, *AfricaRail, 2-6 June,*  
711 *Johannesburg, South Africa* **40**, 147–178.

712 Watkins, S. and Cooper, K. (2007), ‘The unsteady wind environment of road vehicles: part two: effects on vehicle development and  
713 simulation of turbulence’, *SAE Technical Paper* **1(1)**.

714 Watkins, S., Saunders, J. and Kumar, H. (1992), ‘Aerodynamic drag reduction of goods trains’, *Journal of Wind Engineering and*  
715 *Industrial Aerodynamics* **40**, 147–178.

716 Wordley, S. and Saunders, J. (2008), ‘On-road turbulence’, *SAE Int. J. Passeng. Cars - Mech Syst.* **1(1)**.